Reviewed Preprint
v1 • January 5, 2026
Not revised

Reviewed Preprint
v2 • April 28, 2026
Revised by authors

For correspondence:
weiger@biomed.ee.ethz.ch

Competing interests: No competing interests declared

Reviewing editor: Jiang Du, University of California, San Diego, United States

Direct MRI of Collagen

Jason D van Schoor, Markus Weiger, Emily Louise Baadsvik, Klaas P Pruessmann
Institute for Biomedical Engineering, ETH Zurich and University of Zurich, Zurich, Switzerland

eLife Assessment

This **fundamental** work substantially advances our understanding of a major research question: whether collagen can be directly imaged with MRI. The evidence supporting the conclusion is **compelling**, with methods, data, and analyses that are more rigorous than those currently considered state-of-the-art. The work will be of high interest to MR physicists and clinicians, as collagen is the most abundant protein in the human body and plays an essential role in health.

https://doi.org/10.7554/eLife.109799.2.sa4

Abstract

Collagen is the most abundant protein in the human body and has an important role in healthy tissue as well as in a range of prevalent diseases. Medical research and diagnostics hence call for means of mapping collagen in vivo. Magnetic resonance imaging (MRI) is a natural candidate for this task, offering full 3D capability and versatile contrast non-invasively. However, collagen has so far been invisible to MRI due to extremely short lifetime of its resonances. Here, we report the direct imaging of collagen in vivo by magnetic resonance on the microsecond scale. The dynamics of resonance signals from collagen were first assessed in samples of bovine tendon and cortical bone. On this basis, imaging was performed at echo times down to 10 microseconds, yielding collagen-specific depiction by echo subtraction. The same approach was then extended for use in vivo, enabling direct collagen imaging of a human forearm. This capability suggests significant promise for biomedical science and clinical use.

I. Introduction

Accounting for about 30% of protein mass, collagen is ubiquitous in vertebrates and plays an integral role in providing tissue strength, flexibility, and support (1). It is a key constituent of the extracellular matrix in structures such as bone, skin, blood vessels, cartilage, ligaments, tendon, and dentine. Variations in collagen content or structure have a major role in aging and are associated with pervasive diseases such as arthritis and fibrosis. Osteo-and rheumatoid arthritis, in particular, are musculoskeletal conditions that affect a large part of the global population Rheumatoid arthritis is an autoimmune disorder in which the immune system targets the joints, causing inflammation and a thickening of the tissues lining the joints (3). Osteoarthritis is a degenerative joint disease involving the breakdown of cartilage. Both result in collagen degradation and lead to pain, swelling, and reduced joint mobility (3, 4). In contrast, fibrosis is the excessive and uncoordinated deposition of collagen and other matrix proteins and is linked to an impaired healing response to infection or injury (5). It affects most organs, can lead to chronic organ failure, and contributes significantly to global mortality (6). In aging, finally, modifications to the biomechanical and biophysical characteristics of tissue result from the consolidation of collagen (7). Consequently, collagen loses its pliability, malleability, and susceptibility to digestion, thereby compromising the functionality of related organs and tissues.

The critical importance of collagen prompts the need for advanced imaging tools to aid in diagnostics and research of collagen-related diseases. Methods such as x-ray diffraction (8) and electron microscopy (9) are used to evaluate collagen structure and organization on the molecular scale, whilst mass spectrometry can be used to quantify and distinguish different types of collagen

(10). Ex-vivo visualization of bulk collagen is typically achieved using optical techniques like fluorescence and visible light microscopy (11). Other optical modalities such as second-harmonic-generation microscopy have been used to evaluate fibrillar collagen in human tissue in vivo, but only for superficial structures due to limited penetration depth (12). None of these modalities appears to be suited for non-invasive routine use in vivo.

Towards in vivo collagen mapping, MRI is an attractive candidate because it achieves 3D coverage and variable contrast non-invasively and without the use of ionizing radiation. Capturing collagen by ^{1}H MRI requires recording of nuclear magnetic resonance (NMR) signals from the hydrogen atoms of the collagen molecule. Due to the macromolecular nature of collagen, the ^{1}H nuclei, experience strong dipolar coupling and related line broadening (13–15). In NMR studies, linewidths can be narrowed by radiofrequency (RF) decoupling or magic-angle spinning (16). These approaches reveal distinct resonances associated with specific binding sites in the collagen molecule, providing insight into its molecular structure. However, such methods are not suitable for in vivo imaging. As a consequence, collagen signal on MRI systems exhibits a single, very rapid, decay with a relaxation time constant, T_2 (T_2* in collagen macromolecules is dominated by T2, whereas T_2' associated with inhomogeneous broadening is negligible; therfore, within the scope of this work, T_2 is always used for the sake of simplicity), of ~10-20 μs (17–21). Well below the timescales of current MRI techniques, signal lifetimes this short have made collagen effectively MR-invisible (17, 22, 23). Rather, indirect MRI approaches have been employed to study collagen, including the use of collagen-targeted contrast agents (24), magnetization transfer (MT) imaging (25), and collagen-bound water imaging through dedicated short-T_2 techniques with ultra-short or zero echo time (TE) (17, 26–28).

In this work, we report direct collagen MRI, matching rapid signal decay by encoding and detection on the scale of tens of microseconds. Free induction decays (FIDs) are recorded from collagen-rich tendon and cortical bone samples, featuring strong, rapidly decaying collagen signals that are readily distinguished from longer-lived bound-and free-water components. Spatial encoding of data taken with different timings, followed by subtraction, yields collagen images of tissue samples and a human forearm in vivo.

II. Results

A. Collagen magnetic resonance signal detection and behaviour

To explore the collagen MR signal, FIDs were acquired from collagen-rich samples of bovine tendon and bone before and after treatment for removing the sources of water signal (22) (including H-D exchange and freeze drying, see Methods). As shown in Fig. 1, the signals exhibit a rapidly decaying component, which has effectively vanished 40 μs after RF excitation. This signal component is chiefly attributed to collagen based on its agreement with previously reported signal behavior (29–32), the correspondence of the estimated collagen signal fraction to the observed signal contributions (see Supplementary S.I), and the fact that magnetization exchange between collagen and bound water operates in the slow regime permitting their independent observation (see Discussion). This last point is supported by the observation that there is hardly any change in decay rates of the shortest-lived component between treated and untreated samples. In the untreated samples, the rapidly vanishing signal is accompanied by a much slower decaying component that is no longer observed after treatment. This component is attributed to collagen-associated water. The modified signal composition is also observed in the accrued signal phase, the slope of which changes after treatment, indicating dominance by another component of different chemical shift. The different signal behavior of the collagen-bound water in bone and tendon is evidence of different tissue structure. In the treated bone, the signal decays into the noise floor as also reflected by growing noise of the phase. In the treated tendon, a low-amplitude, apparently constant signal is observed, which remains above the noise floor for the displayed duration and which we attribute to fat. A distinct bump is observed in the magnitude of the FIDs at ~20-40 μs for all samples except the untreated tendon. It reflects a subtle oscillation stemming from dipolar coupling of the collagen protons with an interaction in the kHz range (13). Note that

the applied treatment also reduces the amplitude of the rapidly decaying component, indicating that the H-D exchange part of the treatment has also occurred in components with short-lived MR signals due to the presence of exchangeable protons on macromolecules (33).

To more quantitatively investigate the features of the observed FIDs, a representative signal model was found permitting a fit of the decay curves including the observed bump with a limited number of components (see Supplementary S.II). The fitted components describe the overall signal behavior, but do not unambiguously reflect distinct proton pools due to restricted model complexity.

Overall, the observed signal contributions from collagen and water are of comparable order, indicating that the available level of collagen signal can be expected to provide a suitable basis for direct collagen imaging at useful signal-to-noise ratio (SNR). That said, the rapid signal decay poses a significant challenge compared with use of the longer-lived signal of collagen-bound water.

B. Direct collagen MR images are produced using two ultra-short echo times

To enable MRI based on the extremely short-lived collagen signal, very short TEs and rapid spatial encoding were achieved by means of advanced, custom short-T_2 technology including high-performance RF and gradient hardware as well as dedicated imaging methods. Short-T_2 imaging was performed at multiple, increasing TEs in the untreated and treated collagen-rich samples, thus enabling observation of the signal behavior also with spatial localization.

Fig. 2 demonstrates direct collagen imaging, with resulting images displayed for selected early TEs. For the two shortest TEs, all samples are depicted at substantial signal intensity. A decrease in intensity is observed for increasing TEs in all samples, in agreement with the early decay of the collagen signal observed in the FIDs. However, the intensity decrease is less obvious in the untreated samples because the water signal dominates. In both treated samples, the image intensity is significant at the earliest TE of 10.4 μs and rapidly decreases to be nearly unobservable by a TE of 35.4 μs. In addition, obvious blurring effects are visible as compared to the untreated samples, indicating dominance of signals with very short T_2s for which the rapid decay limits the spatial resolution. These findings are consistent with the effective resolution associated with T_2 blurring calculated using the method by Froidevaux et al. (34) (Supplementary S.III). Overall, the observations support the interpretation that the images of the treated samples primarily show collagen.

In Fig. 3, the decay of collagen signal is observed with spatial localization. ROIs are drawn over the same region for all acquired TEs, and the mean signal intensity is plotted for each sample as a function of TE. Overall, the observed signal characteristics match those of the magnitude of the FIDs in Fig. 1. In particular, the rapid initial signal decay and dipolar oscillation are present.

To further support image interpretation and to investigate the potential of in vivo collagen-specific MRI, isolation of the collagen signal was targeted by subtraction of images with different TEs (35–39). This approach is justified by the observation that the signals of the investigated tissue samples exhibit decay times for collagen that are clearly distinct from those of the longer-lived contributions. The shortest-TE image was used to provide the highest contribution from collagen. An image at slightly longer TE was selected to exhibit significant decay of the collagen signal but negligible change of the longer-lived signal components. In this way, high specificity for collagen is achieved at useful sensitivity. Fig. 4 displays the results of selective collagen imaging for untreated and treated samples. In the difference images, the longer-lived water and fat signals are suppressed, leaving only the short-lived collagen signal component. For the treated samples, the subtraction has only a small effect, confirming that the treatment largely removes the longer-living signal contributions and the images mainly show collagen. In tendon, the subtraction removes the fat signal, which was not affected by the treatment. In the untreated samples, subtraction successfully removes the long-lived signals, indicated by the blurrier appearance of the difference images. The slightly sharper depiction of the untreated versus treated samples can be explained by a small amount of residual longer-lived signal. These findings are supported by

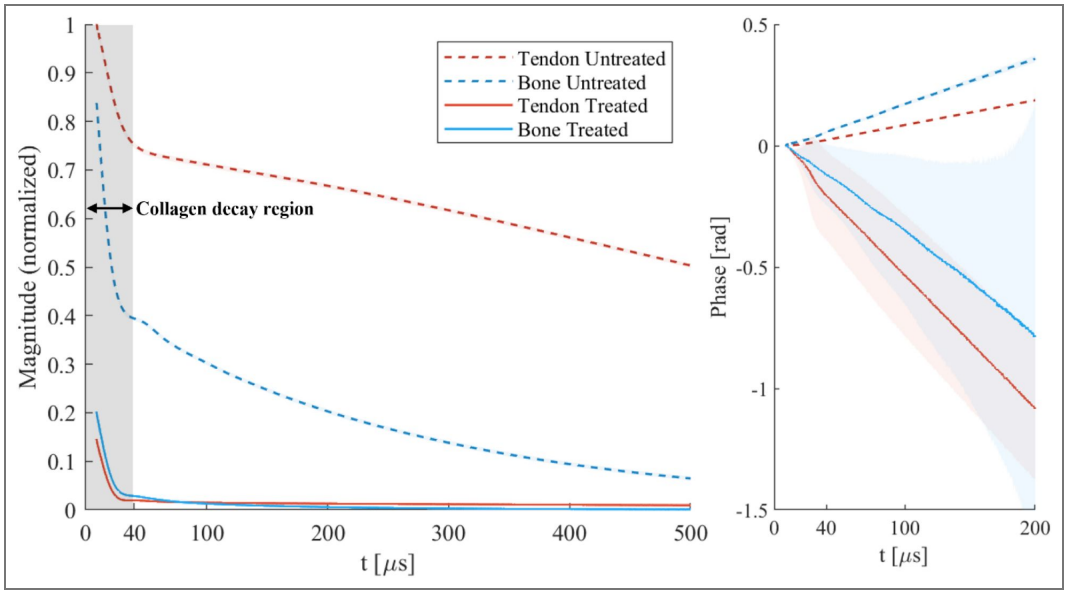

Fig. 1. FID signals of tendon and cortical bone samples before and after treatment with a procedure to remove the water signal.

The magnitude has been normalized by the maximum signal observed in the unprepared tendon. The shaded areas around the lines indicate the 90% central ranges of the averaged data, which are generally very narrow and only large for the phases of the treated samples. A rapidly decaying signal, attributed chiefly to collagen, is observed on top of the slower-decaying collagen-bound water signal for untreated samples. Much longer decaying components from free water and fat are also present but hardly differentiable at this timescale. The collagen component appears to have completely decayed after ~40 μs. The treated bone signal decays into the noise floor, as also seen in the phase of the signal. The treated tendon signal remains above the noise floor due to the presence of longer-living fat signal in the tissue. The distinct bump observed in the magnitude data (for treated and untreated bone, and treated tendon) is attributed to an oscillation stemming from dipolar coupling of the collagen protons. The reduced amplitude of the rapidly decaying component after treatment is believed to be a result of H-D exchange of exchangeable protons on collagen and other molecules with short-lived signals. The variation in phase accrual observed before and after treatment indicates chemical shift differences of the signal contributors that persist post-treatment. The marked collagen decay region indicates the maximum time range available for spatial encoding in direct collagen imaging. In contrast, imaging based on collagen-bound water can utilize the full plotted range.

Fig. 2. **Direct MRI of collagen.**

From an image series of collagen-rich tissue samples with increasing echo times (TEs), four examples at early TEs are shown. The magnitudes are normalized by the maximum signal in the shortest-TE image of the respective sample. A decrease in image intensity is observed with increasing TE, reflecting the decay of collagen signal. In the treated samples, the signal has virtually completely decayed by TE = 35.4 μs. The effect is less obvious in the untreated samples due to strong background signal from water contained in the samples. In the treated tendon sample, the bright fat signal appears constant due to negligible signal decay over the given timescale.

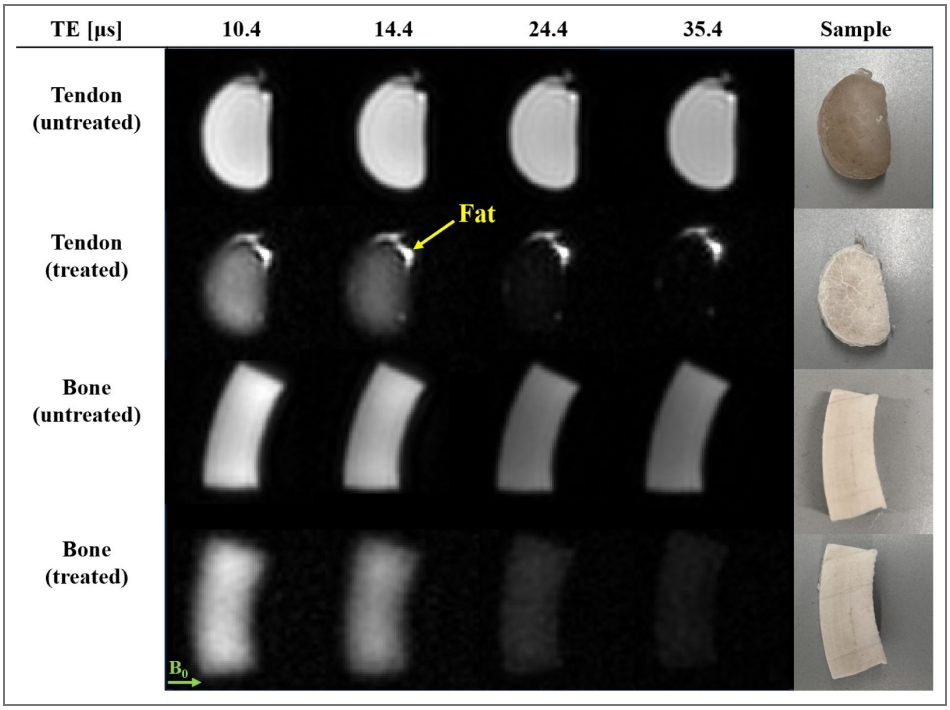

Fig. 3. **Decay of collagen signal observed with spatial localization by imaging at multiple echo times (TEs).**

The magnitude of the mean signal in a region of interest (ROI) in the bone and tendon samples is plotted as a function of TE. The rapidly decaying collagen signal is observed in both the treated and untreated samples. These plots are equivalent to the FID signal magnitudes shown in Fig. 1, including the dipolar oscillation in bone and treated tendon at the interval of ~20-40 μs. However, with imaging, the signal can be observed at specific locations. The shaded areas around the lines indicate the 90% central ranges of the averaged data points.

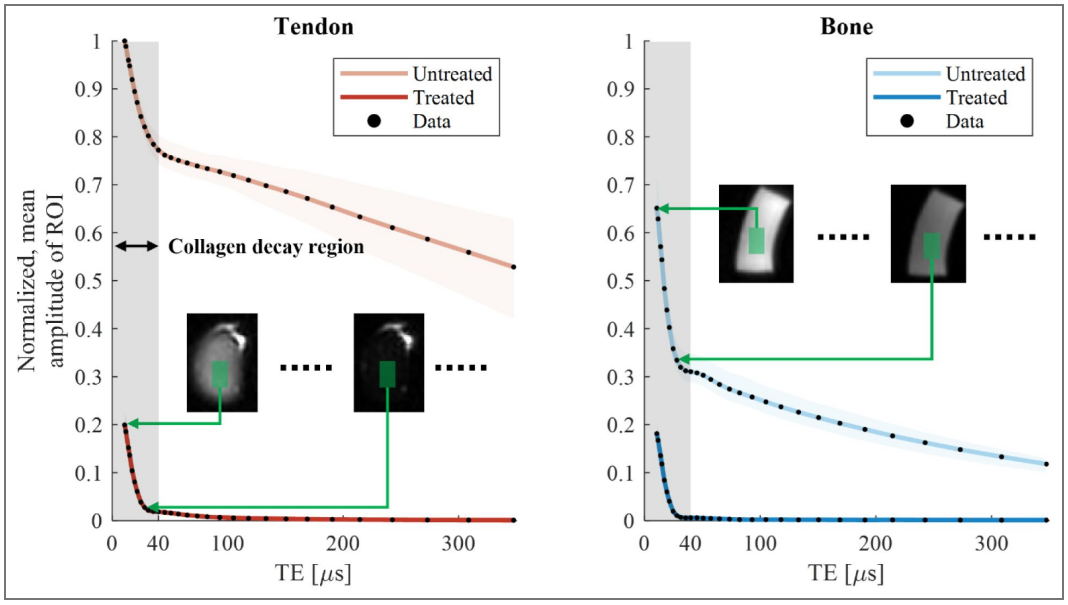

simulations of the full imaging and subtraction procedure based on the initially observed signal characteristics (see Supplementary S.IV). Notably, in the treated tendon, a bright band is observed in the difference image suggesting a change in local tissue structure. A deeper analysis of this observation can be found in Supplementary S.V.

C. Direct collagen MRI can be performed in vivo

For in vivo demonstration, the experimental protocol underlying Fig. 4 was modified for imaging of a human forearm. Fig. 5 shows the two resultant short-TE images and their subtraction indicating collagen content distribution. In the image with slightly longer TE, reduced intensity can be readily observed in cortical bone. Consequently, the difference image shows positive contrast for bones. Furthermore, tendon and skin are visible. In contrast, tissues with long-lived signals such as bulk water in muscle, bone marrow, and other fatty structures are largely suppressed in the difference image. Muscle exhibits a higher intensity after subtraction than signal-void locations (outside the arm) and bone marrow, suggesting that rapidly decaying signal contributions are detected also in muscle tissue. These contributions may arise from condensation of dense connective tissue at the muscle margins, forming tendons or aponeuroses or even from non-collagenous macromolecules such as other proteins and phospholipids (reported T_2 of ~16-25 μs) (21, 40–43).

III. Discussion

The results obtained in this study confirm that direct collagen imaging is possible. In FIDs, collagen signal was identified as a very rapidly decaying component. Spatial resolution of this decay has been achieved using advanced, custom short-T_2 technology and a multi-TE imaging strategy. Collagen signals were captured by the earliest TEs in the series, and image subtraction yielded a collagen-selective depiction both in tissue samples and in vivo.

The FIDs shown in Fig. 1 reproduce the signal behavior of similar tissues in previous works (29–32) where contributions with distinct T_2s are assigned to macromolecular protons and bound water protons, respectively. The independent observation of macromolecular and bound water signals is dependent on the rate of magnetization transfer between the two pools. Using the Bloch-McConnell model (44) outlined by Vallurupalli (45), the magnetization exchange regime is slow if $k << |\Delta R|$, where k is the magnetization exchange rate and ΔR is the difference in the relaxation rates between the two proton pools. With reported values of k for tendon and cortical bone on the order of 1-80 s^{-1} (14, 46) and estimated ΔR on the order of 10^4-10^5 s^{-1}, the magnetization exchange regime is slow and thus macromolecular and bound water signals are indeed separably observable.

We assign the rapidly decaying macromolecular component primarily to collagen according to the expected signal fraction estimated in Supplementary S.I. This component has a T_2 on the order of 10 μs in agreement with previous NMR work (17–21). Additionally, small signal contributions from other macromolecules with T_2s of this order are also expected to be present (18). The difference in magnitude after treatment of the shortest-T_2 component may be a result of H-D exchange with protons in hydroxyl groups or amines of collagen, or on other macromolecules such as hydroxyapatite in bone (33). The rate of decay of the collagen signal between treated and untreated samples appears largely unchanged, further supporting the claim that magnetization transfer between collagen and collagen-bound water has little effect on the observability of the collagen signal. The distinctive bump occurring at ~30 μs is believed to be a dipolar oscillation from interactions between collagen protons. Multiple dipolar coupling phenomena exist within collagen (47), and a superposition of these interactions is observed here. Isolating specific interactions is hampered by low spectral resolution, which is itself a consequence of dipolar coupling. Furthermore, magnetization transfer between collagen protons occurs in the fast regime, and impacts the observed signal decay (14). The slower decaying signals, with T_2s on the order of 100s of microseconds, in the untreated samples are attributed to collagen-bound water. The bound-water signal has completely vanished in the treated samples and only the collagen component remains, suggesting that the treatment to remove water signal was successful. The

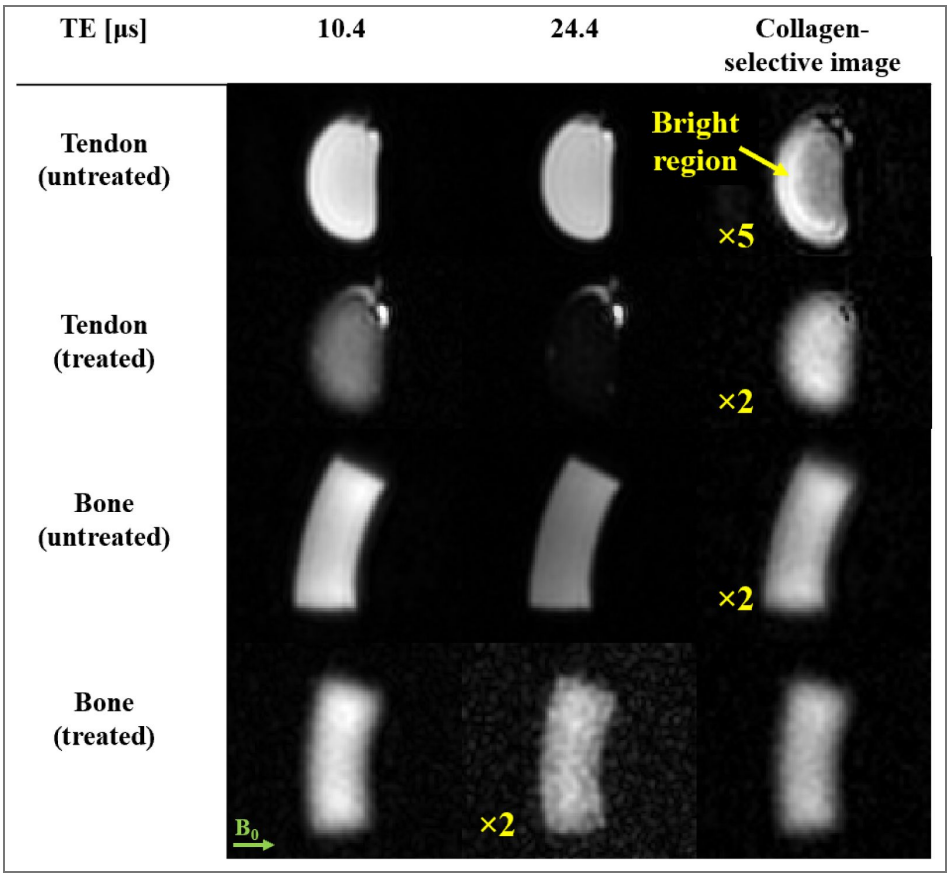

Fig. 4. Selective imaging of collagen in tendon and bone samples.

Isolation of the collagen signal is achieved by subtraction of the shortest-TE image (10.4 μs) and an image with slightly longer TE (24.4 μs). The image intensities have been normalized by the maximum signal observed in the shortest TE image of the respective sample. The bright fat signal in the tendon has been clipped to visualize the collagen in the non-difference images. The images have been scaled, as indicated, for visualization purposes. In the difference images, long-lived water and fat signals are suppressed, leaving only the short-lived components, which are attributed chiefly to collagen. For the treated samples, the effect of subtraction is negligible. The fat signal in treated tendon persists and is removed after subtraction, indicating that the treatment does not impact the fat and that longer-lived signals are suppressed by the subtraction procedure. The difference images of the untreated samples exhibit less T2 blurring than the treated samples due to residual signal contamination from the collagen-bound water signal (Supplementary S.IV). In the untreated tendon, the subtraction yields a bright region that is not visible in the treated counterpart. This suggests an effect of the treatment on the samples that is observable at the collagen timescale.

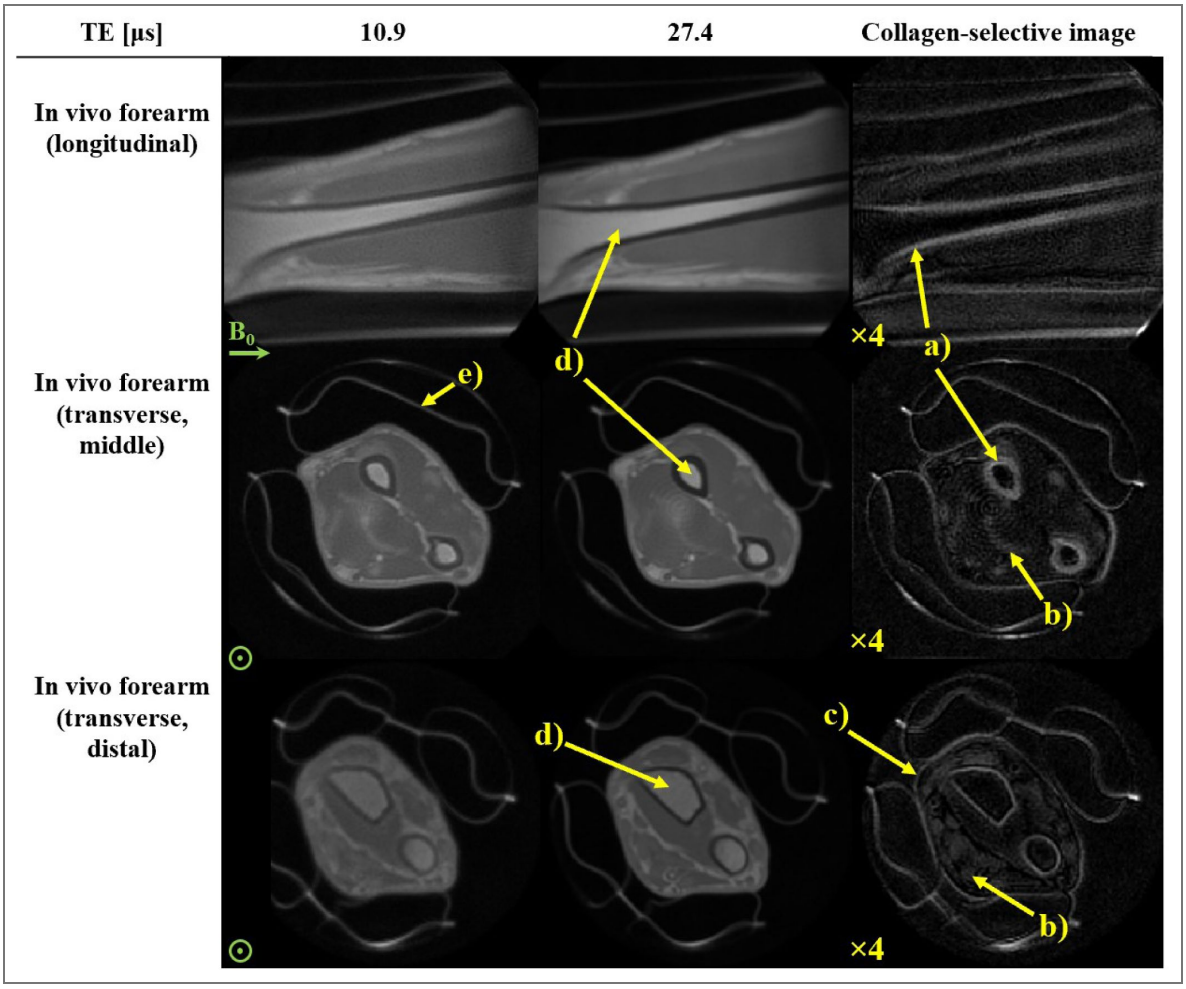

Fig. 5. Direct collagen MRI of a right human forearm in vivo.

Three views of the forearm are shown at two short-TE acquisitions along with the collagen-selective difference image. Images have been normalized according to the maximum signal observed in the earliest TE image of the displayed slices and scaled as indicated. Note that the difference in contrast of the two raw transverse views is due to variations in transmit sensitivity of the RF coil. The difference images show collagen-rich anatomy such as a) cortical bone, b) tendon, c) skin and subcutaneous tissue, whereas longer-lived signals such as from d) trabecular bone are suppressed. Signal from padding, e), is also captured. A slight ringing artifact (typical of high-bandwidth radial acquisitions) is observed in the transverse view.

weak, apparently constant signal component that remains above the noise floor in the treated tendon is assumed to be from residual fat, which is unaffected by the treatment (33) and decays much slower than would be observable at this timescale. Using a model with a relatively small number of components, the FID signals could be well fitted, including the dominating collagen component with dipolar oscillation (see Supplementary S.II). However, the terms describing the dipolar oscillation are rather a simplification of the underlying interactions and on this basis, and extracted signal components from the model are not assigned to specific proton pools. Despite this, excluding the dipolar oscillation and describing the signal as a sum of basic decay functions could still be a viable alternative to extract tissue-specific amplitude components, as suggested previously (29–32). Such efforts have been reported for cortical bone (19) and myelin (48) using spectral- and time-domain modeling, respectively.

The rapid collagen signal decay during an imaging readout is prone to causing significant image blurring (49) (see Supplementary Text S.III). For the current imaging protocols, exponential decay with T_2 = 12 μs for collagen leads to an effective resolution of 2.2 mm as compared to 1.6 mm without decay (34). To contain the blurring effect, short observation times must be achieved by rapid spatial encoding using strong gradients, which comes at an intrinsic SNR expense compared with acquisition at lower bandwidth. The effective resolution can be further improved to some degree by increasing nominal resolution or using longer dead times, albeit at further expense in SNR efficiency (34). Hence, a reasonable compromise between resolution, SNR, and scan time must be found, particularly for in vivo applications. Regarding the critical role of SNR, the results of this work suggest that the large collagen content of tissues of interest affords considerable SNR permitting detailed depiction.

Rapid RF switching and spatial encoding with custom hardware has enabled a multi-TE experiment with very short, continuously selectable TEs. The absence of collagen signal after ~35 μs (Fig. 2) suggests that using TE longer than this is not beneficial for studying collagen directly. In practice, fewer TEs could be used in the multi-TE acquisition to reduce scan time. Alternatively, additional TEs could be acquired at earlier intervals to improve the temporal resolution of signals decaying within these intervals. This could provide the insight required to isolate signal components with similar decay rates to collagen, such as hydroxyapatite in bone.

Both the multi-TE plots and the FIDs suggest that image subtraction between the earliest TE (~10 μs) and a slightly longer TE (~25 μs) is a suitable choice for preserving the rapidly decaying component while suppressing the longer-lived ones (T_2 > 100 μs) (Fig. 4). The use of just two TEs to isolate collagen is advantageous for in vivo applications where minimal scan time is desirable. The subtraction yields an image that predominantly depicts collagen. This has been confirmed based on simulated acquisitions with tissue components according to a signal model replicating the FIDs (see Supplementary S.IV). Increasing the TE interval will increase collagen sensitivity at the expense of specificity. The best trade-off between the two will vary depending on the features to be highlighted. Notably, selective collagen depiction by subtraction worked equally well with treated and untreated samples. This is important for the in vivo scenario where treatment is not an option.

Direct collagen imaging of the forearm in vivo yielded an anatomically insightful image (Fig. 5). Dense, collagen-rich structures such as tendon and bone appear bright while the less dense, collagen-poorer muscle is largely suppressed. The detailed investigation on tendon and bone samples, in which collagen dominates as a contributor to the shortest T_2s, supports the interpretation of the in vivo data as reflecting collagen density with high specificity. Overall, image SNR was found to be remarkably good (~24.9 for cortical bone and ~16.6 for tendon – see Supplementary S.VI) considering the extreme timescale of signal encoding, acquisition and decay. For skin and muscle, which are also depicted in the collagen image, the origin of the short-T_2 signal is likely collagen with additional macromolecular contributions that remain to be clarified. Other anatomies (such as the knee and ankle) and tissues (such as dura and dentin) are collagen-rich and of interest for future in vivo studies with the same setup as used in this work. Direct collagen imaging is a promising method also for the study of fibrosis. Thus far, in vivo MR studies of fibrosis are limited to indirect methods such as MR-elastography (50) and MT (51). Direct

collagen imaging in fibrosis is of clinical interest particularly in the torso, calling for high-performance whole-body gradients. Ongoing advances in gradient engineering are achieving adequate amplitudes (52). However, full duty-cycle, as required for efficient collagen imaging, has yet to be achieved with whole-body, high-performance designs. So far, conventional clinical MRI systems lack the capability of sustained high gradient strengths and rapid RF switching as required to image collagen directly. However, small-bore preclinical MRI systems often offer advanced gradient and RF capabilities, making them potentially more suitable for direct collagen imaging in ex-vivo samples as well as for in vivo small animal models. Nevertheless, gradient duty cycle limitations must still be taken into consideration. Another limitation for in vivo imaging can be the high RF power deposition of the high-bandwidth excitation required by the sequence. Although not the case in the presented example, this can effectively restrict the excitation flip angle and thus SNR, depending on the particular anatomy and RF coil (49, 53). In this respect, new developments for reducing the specific absorption rate are promising (54).

In conclusion, MRI has the capacity to image collagen directly when performed at the timescale of T_2 on the order of 10 μs. This is possible with high-amplitude, full-duty-cycle gradient instrumentation, fast RF switching, and targeted acquisition protocols as derived here from initial characterization of the collagen signal. Direct collagen MRI has the potential to open a new field of research as well as clinical applications. It will be instrumental to quantitative studies on collagen-rich tissues in vivo, in which the macromolecular fractions have so far been determined only indirectly (55). The ways in which pathology manifests in collagen images remain to be seen and could be investigated using studies on manipulated and pathological tissues. However, the ubiquity of collagen, its role in prevalent diseases, and the ability to image it with nuance and adequate SNR suggest significant diagnostic promise.

IV. Materials and Methods

A. Preparation of collagen-rich samples

Bovine Achilles tendon and femoral bone (~80% and ~25-30% collagen type I by dry mass, respectively (56, 57)) were acquired from a local butcher. The specimens were cleaned of excess fat and muscle tissue. The bone marrow was removed, and a section of cortical bone was cut using a saw. Tendon and cortical bone samples were cut to approximately 10 x 25 mm^2. The samples were stored frozen before being thawed and brought to room temperature for the imaging experiments. The samples underwent a procedure to largely remove the sources of the water signal in the MR experiments (22). The procedure used D_2O exchange for 4 days (replacing the D_2O after 2 days) followed by freeze-drying the samples for 3 days. In this way, water molecules should either be removed from the sample or not provide ^1H signal. The MR experiments were performed on the same samples before and after the procedure and are referred to as “untreated” and “treated”, respectively. Care was taken to place the samples in the same orientation with respect to the main magnetic field to avoid signal changes due to orientation.

B. NMR & MRI experiments

MR experiments were performed on a 3T Philips Achieva system (Philips Healthcare, the Netherlands) equipped with a custom gradient capable of reaching a strength of 220 mT/m at 100% duty cycle in a bore size of 33 cm (34), and rapid transmit-receive switches (58). Samples were studied using an RF loop coil of 40 mm diameter, and the in vivo experiment was performed using a quadrature birdcage coil of 100 mm diameter (59). Both RF coils have been designed to largely avoid ^1H background signal from their materials.

FIDs were acquired on the tendon and bone samples. The purpose of acquiring the FIDs was to observe the overall signal behavior as well as to characterize tissue components for further experiments and simulations. The FID protocol was as follows: 2 μs block pulse, flip angle of 30°, repetition time (TR) of 30 ms, and 10 000 signal averages.

MR imaging was performed using a pulse sequence known as pointwise encoding time reduction with radial acquisition (PETRA) (60), which is a zero echo time-based technique (61) in which the central gap in k-space is acquired using single-point imaging (62). The gap given in Nyquist intervals is defined as kGap = DT × BW, where DT is the dead time and BW is the imaging bandwidth (see Fig. 6) (48). The sequence was performed on the samples with DT ranging from 10-321 μs to observe the signal behavior with spatial localization. The bandwidth was adjusted such that the gap was constant for all acquired DTs. The effective TE values were assigned as TE = DT + Δ, where Δ accounts for averaging oversampled data over a Nyquist dwell 1/BW. This assignment was found to be appropriate by means of simulations (see Supplementary Text S.VII).

In vivo experiments were performed in the forearm of a male volunteer after written informed consent and in agreement with regional ethics regulations. The arm was immobilized by means of inflatable cushions. Two TEs of 10.9 μs and 27.4 μs were chosen based on the results of the FID and multi-TE acquisition of the samples as well as simulations. The imaging parameters are shown in Table 1.

C. Data processing

Raw data was demodulated at the water frequency to prevent off-resonance blurring at lower BWs. At the associated larger TEs, the off-resonant collagen signal has already decayed sufficiently to consider its contribution negligible. Images were reconstructed by iterative k-space re-gridding (64) and application of a hyperbolic secant windowing function (exponent 10, truncation factor 5) (48, 65) to remove Gibbs ringing effects from slower decaying signals. To observe the signal behavior of certain locations in the samples, ROIs were selected and the mean signal intensity was plotted as a function of TE. From these plots, two TEs were selected to perform image subtraction for preserving the shortest-living component while suppressing the longer-living components in the samples (35–39). The selected TEs also served as a guide when choosing imaging parameters for the in vivo application, where image subtraction was performed after registering the images. In the subtraction image, negative values were set to zero (66). For visualization purposes and SNR calculations, a two-fold bi-cubic interpolation was applied, and the average over three neighboring slices was performed for the in vivo case.

Fig. 6. The short-T2 PETRA protocol employed for direct collagen MRI.

a) Basic zero echo time (ZTE) pulse sequence. After the RF dead time (DT), radial encoding is performed to collect either ZTE data along radial spokes in k-space or single-point-imaging data to fill the central k-space gap caused by the DT. b) Corresponding t(k) plot, showing the time after excitation when each k-space data point is acquired. Inside the gap, the SPI data forms a plateau, whereas outside, the ZTE data forms a linear increase. To observe signal decay, the DT is increased in successive imaging experiments. The k-space gap (kGap ∝ DT × G) is kept constant by reducing the gradient strength, leading to a steeper slope of t(k).

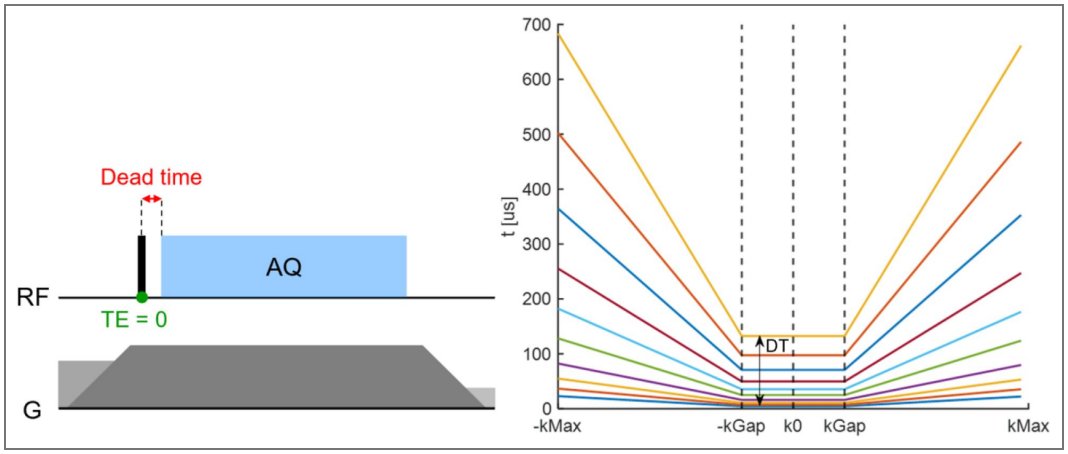

Table 1. Parameters for multi-TE imaging of collagen-rich samples and in vivo human forearm.

Abbreviations: TE, echo time, TR, repetition time, BW, image bandwidth

Protocol	Samples	In vivo forearm
TE (μs)	10.4-347.4	10.9, 27.4
BW (kHz)	598-18.7	1215, 486
Excitation pulse	2 μs block, 5.7°	2 μs frequency-swept (63), 2.7°
TR (ms)	3.0	1.0
Field of view (mm)	64	130
Nominal resolution (isotropic) (mm)	1.0	0.98
Scan time per image (m:s)	02:00	09:38

Supplementary Materials

I. Estimation of contributions to proton signal

Contributions from different tissue components to the MR signal are estimated here through the approximation of the proton count associated with the principal proton-containing compounds found in tendon and cortical bone tissues. This analysis supports the attribution of the dominant, rapidly decaying signal component largely to protons on the collagen molecule.

The number of protons per gram is calculated as:

$$\frac{\text{protons}}{g} = \frac{\mathrm{N_a}}{MW} \times \frac{\text{protons}}{\text{molecule}} \tag{S1}$$

Where N_a is Avogadro's number and MW is the molecular weight in g/mol. The results are listed in Table S1.

To estimate the signal contributions for a specific tissue, the proton counts of the compounds are weighted by their percentage per mass in the tissue. For tendon we assume 63% water and 27% collagen by mass according to Taye et al. (67). The remaining 10% comprise elastin and other extracellular proteins which are not considered here. For cortical bone we assume 8% water, 22% collagen and 70% hydroxyapatite by mass taken from Auget and Schorlemmer (68).

By normalization, the estimated signal fractions are obtained as shown in Table S2. Protons from collagen contribute a significant proportion of the total MR signal in both tendon and cortical bone – 21% and 59% respectively. Notably, hydroxyapatite has a low proton density and thus contributes little to the signal in cortical bone, making collagen the dominant contributor to the rapidly decaying signal.

Compound	Chemical formula	Protons/ molecule	Molecular weight (MW) [g/mol]	Protons/g [10^{21}]
Collagen chain of Glycine-Proline-Hydroxyproline	$C_{12}H_{19}N_3O_5$	19	285.3	40.1
Water	H_2O	2	18.0	66.9
Hydroxyapatite	$Ca_5(PO_4)_3OH$	1	502.3	1.2

Supplementary Table S1. Dominant compounds in tendon and cortical bone with relevant stoichiometric parameters. The collagen chain of Glycine-Proline-Hydroxyproline is used since it is the most commonly occurring chain in collagen type I (68).

Tissue	Water	Collagen	Hydroxyapatite
Tendon	0.79	0.21	0
Bone	0.36	0.59	0.05

Supplementary Table S2. Estimated signal fractions for tendon and cortical bone tissues.

II. FID signal representation and fitting

Previous studies have modelled FIDs as a sum of decay functions, which produce the established T_2s for collagen and bound water protons. However, this approach does not capture the characteristic dipolar oscillation arising from dipolar coupling (13). Quantum filtered experiments

isolate the collagen component as a doublet with splitting frequencies on the order of 10s of kHz (14,15). This splitting can be modelled using a cosine term leading to the following signal model:

$$S(t) = e^{i\emptyset}\left[\sum_j a_j e^{i\Delta\omega_j t}\cos\left(2\pi f_i t\right) e^{-\left[\frac{t}{T_{2,j}}\right]^{E_j}}\right] \quad \text{(S2)}$$

$\emptyset$ represents a global phase shift, a signifies a component amplitude, $\Delta\omega$ indicates off-resonance due to chemical shift, f represents the splitting frequency of the net dipolar-coupling effect, T_2 denotes a transverse decay parameter, and E represents an exponential coefficient. The exponent E can be varied from 1 to 2 to hybridize the line shape associated with the decay to between Lorentzian (common for solution NMR) and Gaussian (common for solid-state NMR) (70). For non-coupling components, the values of f and E can be fixed at 0 and 1, respectively.

Fig. S1 presents the result of fitting the FID of untreated bone using the model of Eqn. S2. The resulting component parameters are shown in Table S3. Two of the components exhibit rapid Gaussian-like signal decay with dipolar coupling. Similarly, Fig. S2 presents the fitting for the treated tendon sample using three rapidly decaying components (two Gaussian-like with dipolar coupling effects) listed in Table S4. In both cases, the short-lived collagen components are the largest contributors to the signal.

Notably, the net observed coupling phenomena is well described using the mathematical model and proves useful in isolating signal constituents. However, there are limitations in using this technique. Fitting a sum of exponentials, without good priors, is known to be an ill-conditioned problem yielding many plausible solutions. For instance, changing the number of components and allowed T_2s and amplitude ranges will alter the result. It therefore is not appropriate to unambiguously assign signal components to distinct proton pools. Furthermore, the model does not account for effects such as orientation, which has been shown to influence the collagen-bound water signal (70). Nevertheless, the modelling method is sufficient to inform simulations to further probe the possibility of direct collagen imaging.

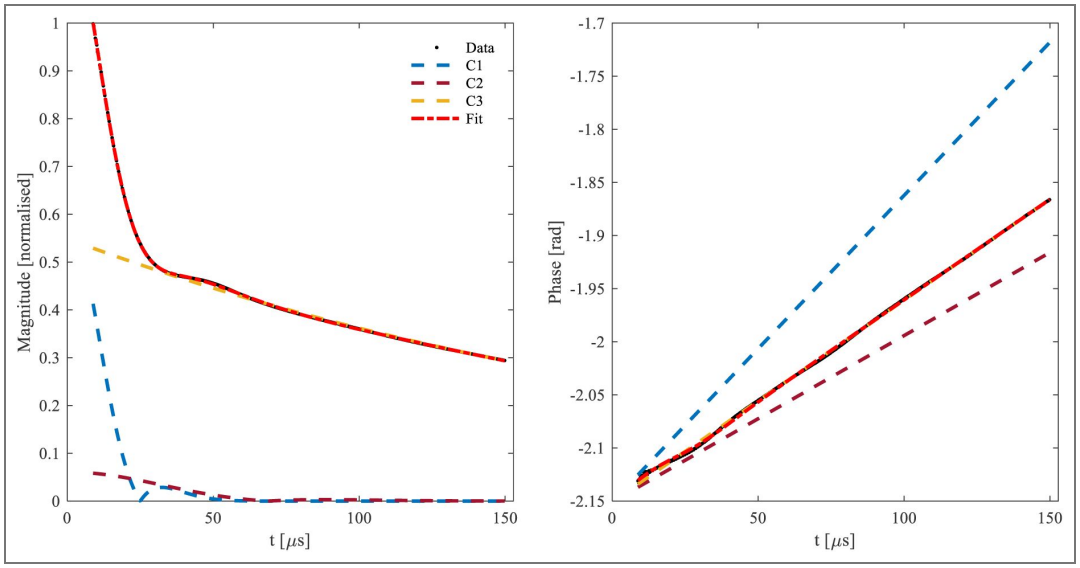

Supplementary Figure S1. FID of untreated cortical bone sample with the accompanying model fit. The bump in the magnitude is attributed to an oscillation from dipolar coupling of the collagen protons. The model fits the data well using three terms, of which two components (C1 and C2) are rapidly decaying dipolar coupling terms.

Component	Amplitude a [norm.]	Off-resonance $\Delta\omega$ [kHz]	Splitting freq. f [kHz]	Decay constant T_2 [µs]	Exponent E
C1	0.497	0.459	10.000	20.7	1.800
C2	0.050	0.249	3.633	60.0	2.000
C3	0.453	0.302	**0**	239.8	**1**

Supplementary Table S3. Components from the fit in Fig. S1. The amplitudes are normalized according to the maximum signal observed in the FID. Notably, the short-lived components make the largest contribution. The values shown in bold were fixed during the fitting procedure.

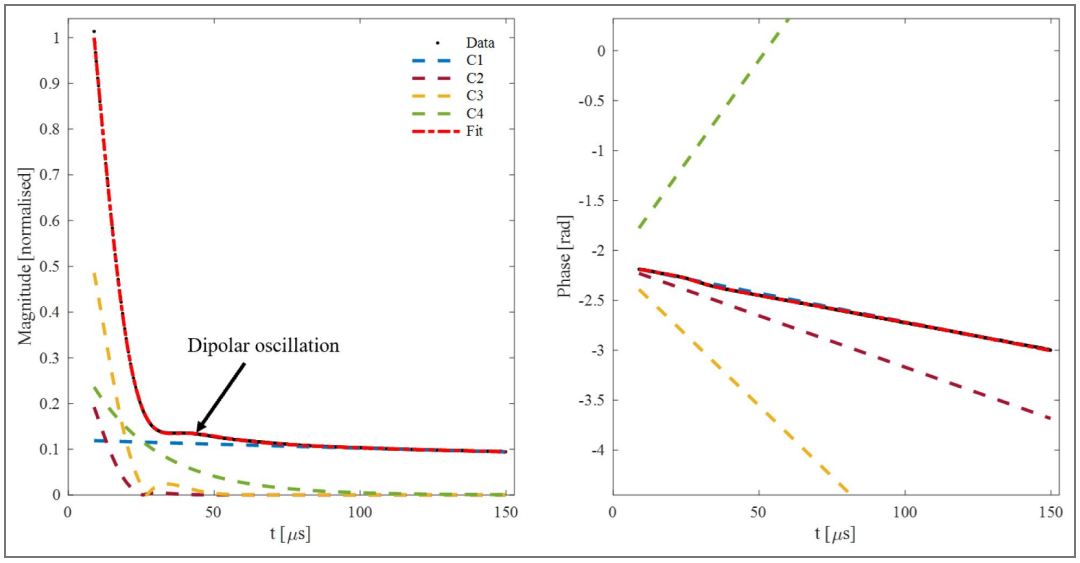

Supplementary Figure S2. FID of treated tendon sample with the accompanying model fit. Again, the bump in the FID from dipolar coupling is preserved. The model fits using 4 terms with C2 and C3 being rapidly decaying components.

Component	Amplitude a [norm.]	Off-resonance $\Delta\omega$ [kHz]	Splitting freq. f [kHz]	Decay constant T_2 [µs]	Exponent E
C1	0.083	-0.936	**0**	594.0	**1**
C2	0.227	-1.630	9.397	17.3	2.000
C3	0.517	-3.700	9.942	20.9	1.848
C4	0.172	7.00	**0**	24.9	**1**

Supplementary Table S4. Components from fit in Fig. S2. The amplitudes are normalized according to the maximum signal observed in the FID. Here, the short-lived components dominate. The values shown in bold were fixed during the fitting procedure.

III. Calculation of T2 blurring

As is well-known in MRI, the time spent on encoding and acquiring signal with respect to T * or T decay impacts both SNR and effective resolution. This aspect is particularly important when imaging tissues with very short T_2 (34,38), where longer encoding times lead to increased T_2 blurring, corresponding to a reduction in effective resolution. For a desired nominal resolution, a large gradient strength enables a reduction in encoding time and is therefore key to contain resolution loss in short-T_2 MRI.

Here, we analyze the resolution of the collagen signal using the method presented for the PETRA pulse sequence by Froidevaux et al. (34). This method assumes an exponentially decaying signal rather than the Gaussian-like decay for collagen modelled in Supplementary Text 2. Therefore, we first derive a corresponding T_2 of an exponential decay from the fitted decay, T^E and exponent, E, which are used to describe the Gaussian-like decay:

$$e^{-\frac{t}{T_2}} = e^{-\left[\frac{t}{T_2^E}\right]^E} \tag{S3}$$

$$T_2 = T_2^E t^{1-E} \tag{S4}$$

Eqn. S4 is plotted in Fig. S3 using the parameters acquired from the modelled bone FID (Table S3). One observes that the equivalent exponential T_2decreases with increasing time. Here, we choose t = 40 µs, which is late in the encoding time of the sequence with a dead time of 10 µs and therefore represents a worst-case scenario of T_2 blurring. t = 40 µs is also the time at which the collagen signal appears to have decayed in the FIDs. The derived T_2 for collagen signal in bone is therefore taken to be 12 µs.

Calculations of effective resolution were conducted for the protocol with the shortest TE in Table 1 and the parameters summarized in Table S5. The associated point-spread-functions (PSFs) without and with T_2 decay are shown in Fig. S4. The full-width-at-half-maximum (FWHM) of the PSF is interpreted as the effective resolution. Without decay, this amounts to 1.6 mm, which is an increase of 60% with respect to the nominal resolution of 1 mm due to the width of the main lobe of the intrinsic, sinc-shaped PSF. For collagen, a FWHM of 2.2 mm is obtained, which is an increase of 38% with respect to the ideal case due to T_2 blurring. This calculation shows that whilst rapidly decaying signals are spatially resolvable, a significant amount of T_2 blurring is to be expected.

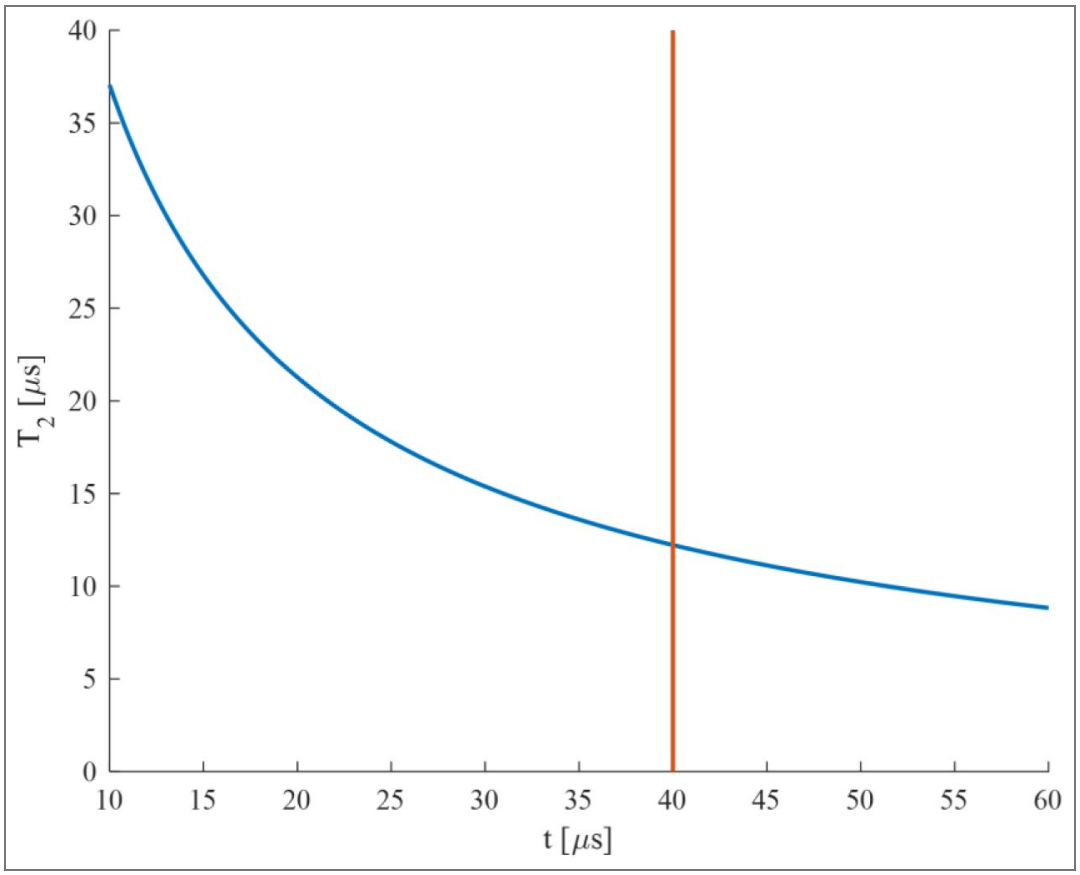

Supplementary Figure S3. **Exponential T_2 as a function of time t according to Eqn. S4 for Gaussian-like decay for parameters $T_2^E = 20.7$ µs and E = 1.8 (the fastest decaying component in Table S1).** One observes that the equivalent exponential T_2 decreases with increasing time. At the indicated t = 40 µs, T_2 is approximately 12 µs.

T_2 [µs]	Gradient Strength [mT/m]	Dead time DT [µs]	Nominal resolution [mm]
12	220	10	1

Supplementary Table S5. **Parameters used for calculation of T_2 blurring.**

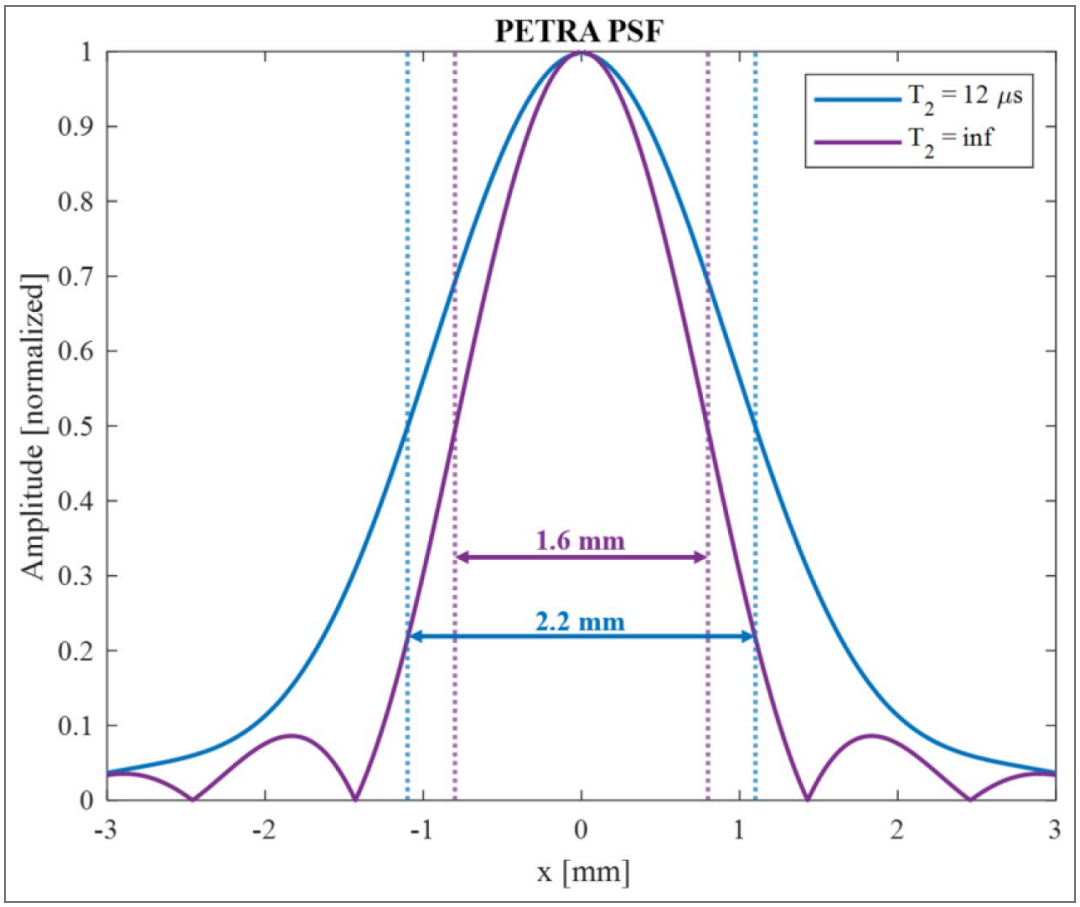

Supplementary Figure S4. **PSF of PETRA pulse sequence for collagen signal with exponential T_2 decay of 12 μs, compared to that of a non-decaying signal, using imaging parameters listed in Table S3.**

IV. Simulation of imaging and image subtraction

To investigate the specificity of image subtraction, i.e., potential contamination by residual water signal in the difference image, simulations were performed. Four spherical objects with distinct T_2 pools were simulated, where three spheres represent individual components and the fourth sphere the sum of all components. The same multi-TE PETRA sequence as in the imaging experiments was applied.

Fig. S5 presents the simulation results. The collagen component is visible at TE = 10 μs and no longer visible at TE = 25 μs. The signal intensity of the bound and bulk water components appears unchanged between the two echoes. Subtracting the two images leaves only the collagen signal component. Merely a very weak residual signal from the bound-water component is observed. Taking the mean image intensities over ROIs in the spheres and plotting them as a function of TE reconstructs the FIDs of the individual and the combined tissue components. It is evident that in the early TE data, the rapidly decaying collagen component is captured. Intensity profiles of the simulated spheres were merged for display to show the effects observed in the images more quantitatively. The effects of T_2 blurring in the collagen sphere are obvious. In contrast, the bound-water sphere does not exhibit blurring, in particular not its contamination to the difference image. This contamination adds to the collagen signal in the combined-signal sphere, resulting in an apparently higher resolution of collagen in the difference image.

The simulations show that the PETRA pulse sequence successfully captures and spatially resolves the rapidly decaying collagen component, and that the collagen signal no longer contributes to images after TE = 50 μs. This would suggest that future investigations that seek only to study direct collagen signal could become more time efficient by excluding longer echo times. Image

subtraction of early echo times convey that primarily the collagen signal component remains, with a small residual contamination from bound water signal (signal with T_2s on the order of 100s of microseconds).

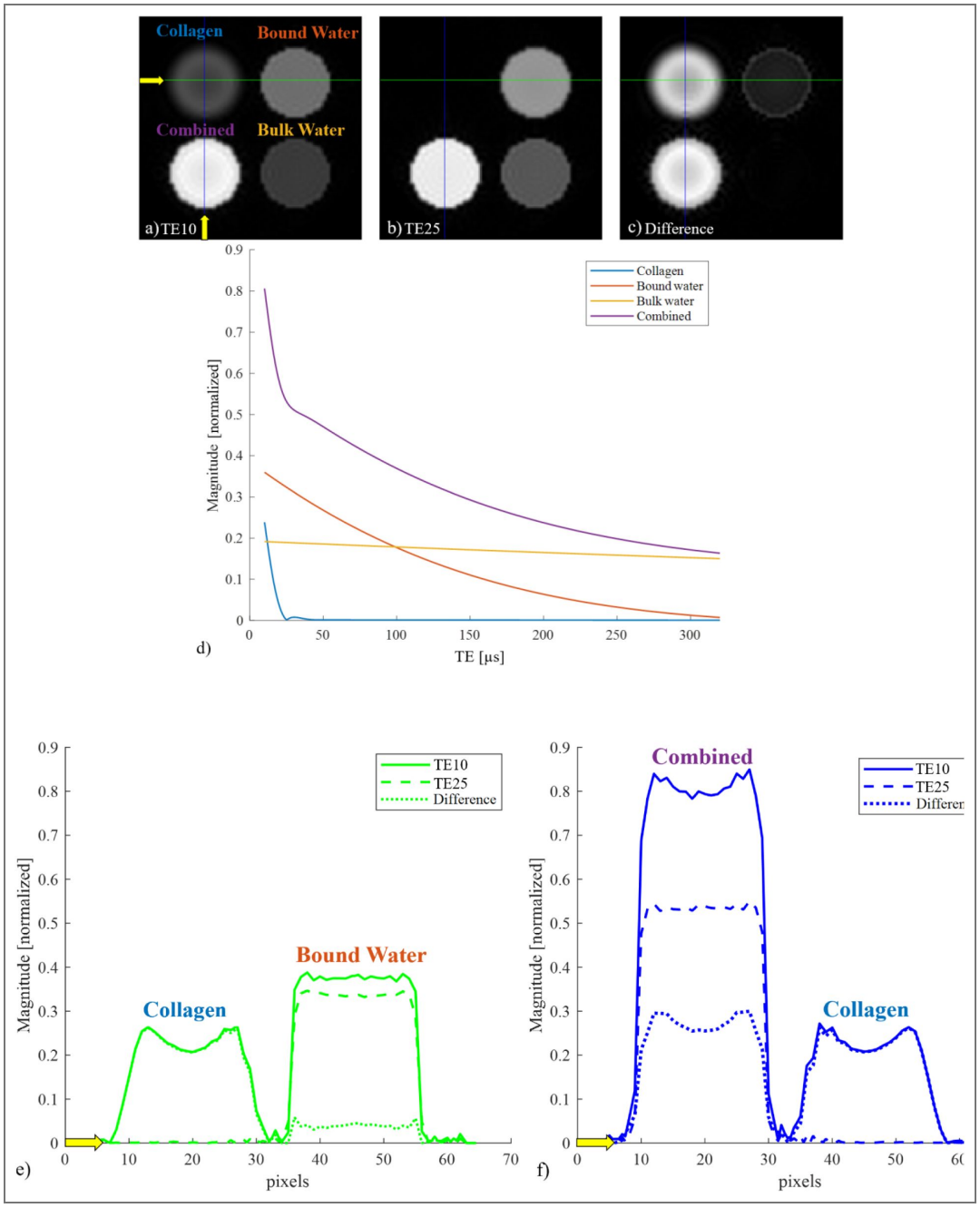

Supplementary Figure S5. Imaging simulation of four spheres using collagen, bound-water, and bulk-water signal characteristics. (i) a "Collagen" component with dipolar coupling (T2 = 10 μs, f = 10 kHz, E=1, Δω = 0.5 kHz), (ii) a "Bound water" component (T2 = 100 μs, f = 0.7 kHz, E=1), (iii) a "Bulk water" component (T2 = 1.3 ms), and (iv

) all components combined (adding all components into a single sphere). The spheres were simulated with a PETRA sequence with TE ranging from 10-320 µs. The displayed images are scaled with respect to their own maximum intensity. a) Simulated image at TE = 10 µs. The collagen sphere shows reduced signal and significant blurring. b) Simulated image at TE = 25 µs. The collagen sphere has vanished while the other spheres persist. c) Difference image of TE = 10 µs and TE = 25 µs. Only the collagen component remains. In addition, a residual ring of the intermediate component is observed, indicating a small signal contamination of ~4%. This ring also appears in the combined sphere, making it slightly sharper than the pure collagen sphere. d) Plotted mean signal intensities over the ROIs drawn over the different spheres as a function of TE. The behavior of the underlying FID signal is reproduced, including the rapid initial signal decay as captured by the shortest TEs. e) and f) Intensity profiles along spheres, illustrating effects of T2 blurring. The profiles show that the collagen sphere is notably more blurred than the bound-water and combined spheres. Furthermore, one observes that the contamination from the bound water adds to the difference profile of the combined signal sphere, resulting in a sharper-looking image. This explains why the T2 blurring from the collagen-only sphere appears more apparent.

V. Multi-TE analysis of untreated tendon

To further analyze the peculiar contrast in the subtraction image (see Fig. 4 of main text) of the untreated tendon sample, the full signal decay is investigated. ROIs are drawn on two different regions of the sample and the mean signal intensity is plotted as a function of TE. The locations of the ROIs are informed by the bright band seen in the difference image shown in Fig. S6, d).

Fig. S6 shows that the initial signal amplitude differs between the two regions, the initial decay is stronger in the bright region, and their signal behavior further changes for TEs above 150 µs (the bound-water imaging interval). These observations indicate the presence of different tissue structures in the sample that – by means of the employed imaging approach – are observable at both the collagen and bound-water timescales. However, the exact mechanism behind this change of signal behavior is uncertain and would need a detailed analysis of the tissue. Notably, the same contrast is not visible in the subtraction of the treated sample, indicating that the treatment leads to changes in the tissue affecting the rapidly decaying signal. Overall, the results show that the direct collagen imaging technique is sensitive to changes in underlying tissue structure, which demonstrates its potential for in vivo MSK diagnostics.

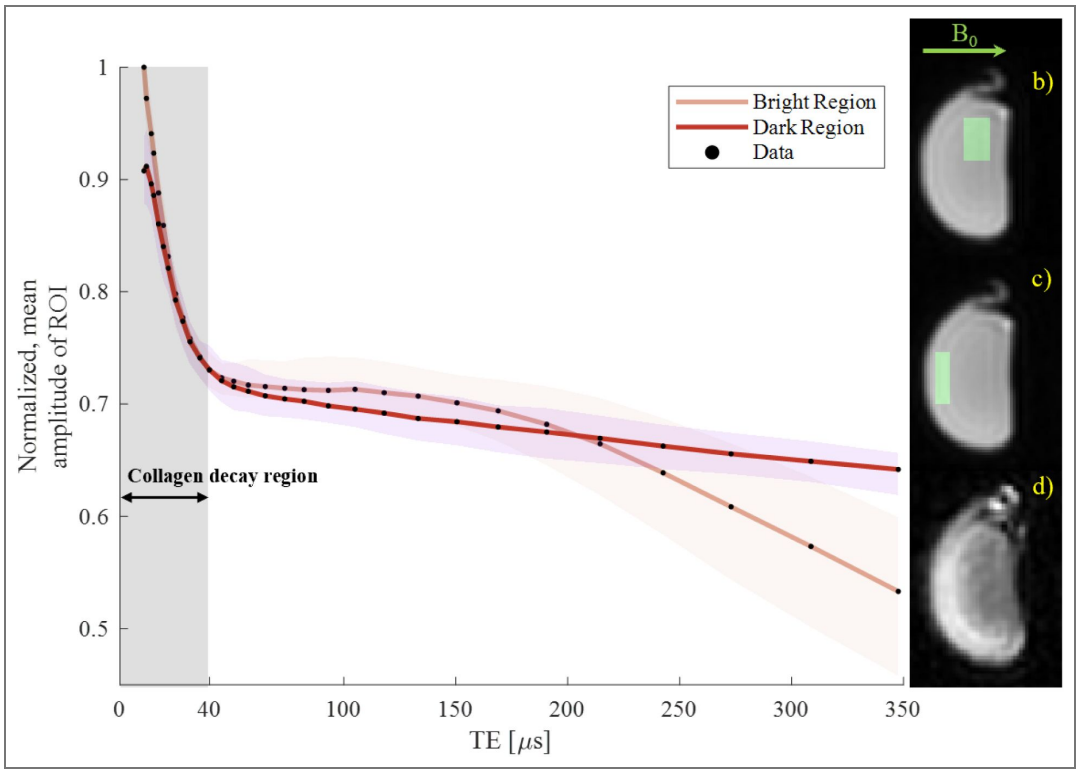

Supplementary Figure S6. Mean signal intensity as a function of echo time (TE) over regions of interest (ROIs) in different parts of the untreated tendon sample. The signal in the bright region of the difference image d) (ROI shown in panel c) for the TE = 10.4 μs image) starts at a larger amplitude, initially decays faster, and shows a change in bound-water behavior after ~150 μs as compared to the darker region (ROI shown in panel b) for the TE=10.4 μs image). This change in signal characteristics is hypothesized to be a result of variation in tissue structure. The shaded areas around the lines indicate the 90% central ranges of the averaged data points.

VI. Determination of SNR for the in vivo collagen image

To determine the SNR of the in vivo collagen subtraction image of the forearm, circular ROIs were drawn over the cortical bone and tendon structures, as well as over areas of pure noise. The SNR was then calculated in the magnitude image as the average intensity of the voxels in the structure $\bar{S}$, divided by the standard deviation of the noise $std(N)$, i.e., $SNR = |\bar{S}|/std(N)$. Before calculating the SNR, as for the visualization, three neighboring slices were averaged. The results are shown in Fig. S7

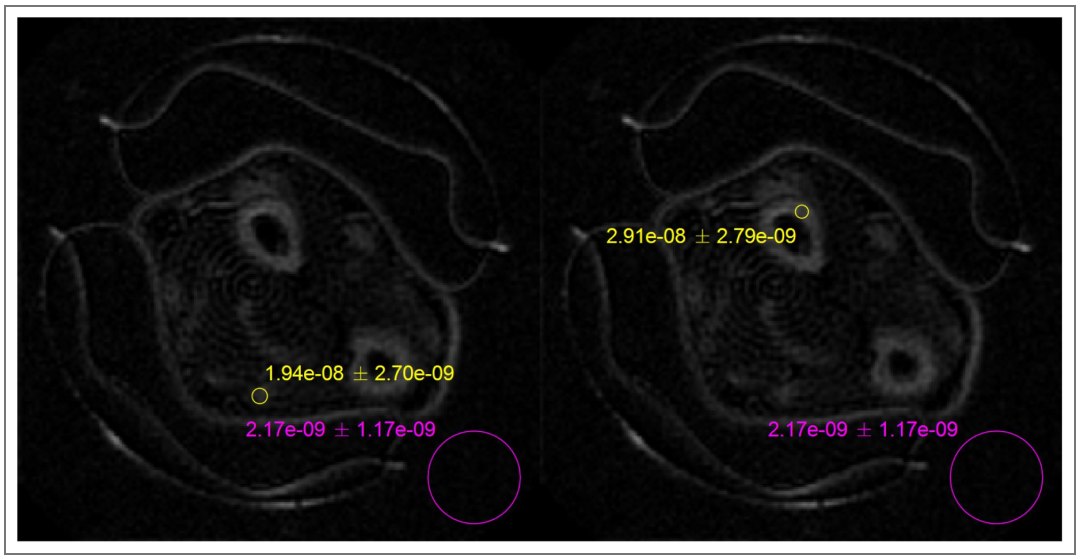

Supplementary Figure S7. ROIs drawn on collagen image of in vivo forearm for tendon (left) and cortical bone (right) structures. Anatomical ROIs are shown in yellow, and the noise ROIs are shown in pink. The SNR is calculated to be 24.9 and 16.6 respectively, including the three-slice averaging used for visualization.

VII. Confirmation of TE assignment

To assign a representative TE for an image with a given dead time (DT, the time between RF excitation and acquisition) for the PETRA pulse sequence, simulations of a single point imaging (SPI) acquisition with the same four spheres as described in *Section II* were performed (60,71). An SPI acquisition collects each k-space point with the same time delay after the RF excitation, and therefore all points have the same T weighting. For SPI acquisitions, we assign $\Delta = \left(\frac{1}{2} - \frac{1}{2ov}\right)\frac{1}{BW}$ accounts for averaging data, which were oversampled with a factor *ov*, over a Nyquist dwell 1/BW. For direct collagen MRI, pure SPI is not practically implementable due to the high gradient demands for larger k-space values. However, simulations allow one to compare the differences in signal magnitude between the acquisitions and then determine a correction factor for the DT of the PETRA pulse sequence such that a representable TE can be assigned (48).

The results of simulating the SPI acquisition as well as the difference in signal magnitude to the PETRA acquisition (from simulations performed and displayed in Fig. S5) are shown in Fig. S8. The SPI signal magnitudes prove to be very similar to those of the PETRA simulations with a very small difference in signal. For this reason, one may assign the TE for PETRA to be:

$$TE_{PETRA} \cong TE_{SPI} \tag{S5}$$

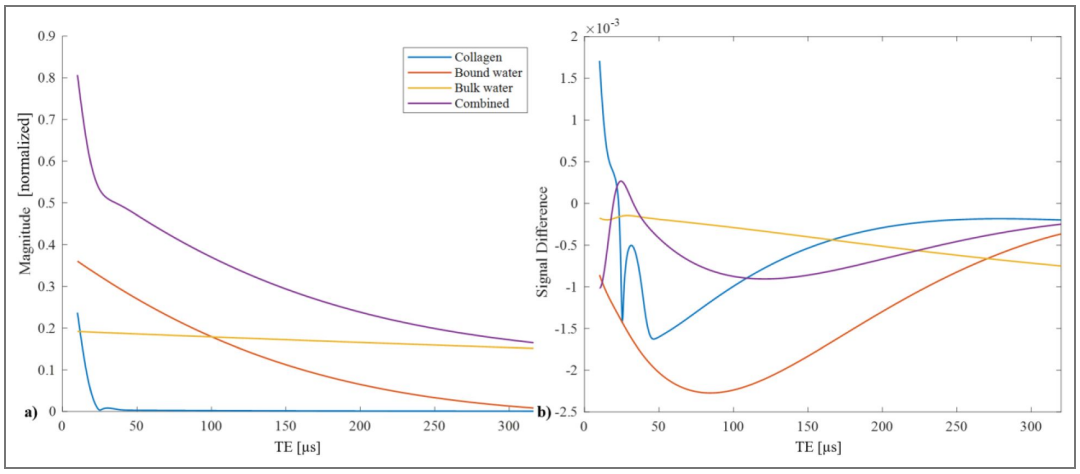

Supplementary Figure S8. Comparison of TEs between Petra and SPI acquisitions. a) ROI plot for simulated SPI acquisition using the same four spheres presented in Fig. S5. The simulated SPI acquisition yields uniform T_2 weighting to all points in k-space and its TE is assigned as TE = DT + Δ. b) difference between signals of different components in the SPI and PETRA acquisitions. The signal difference is small, and this supports the same assignment of TE for the PETRA pulse sequences as for the SPI pulse sequence.

Data availability

MATLAB (MathWorks, USA) analysis code and data is provided at *https://doi.org/10.5281/zenodo.15928442*. All other data needed to evaluate the conclusions in this paper are present in the paper and/or the Supplementary Materials.

Acknowledgements

The authors would like to thank Prof. Matthias Ernst at the department of Chemistry and Applied Biosciences at ETH Zurich for sharing his expertise in solid-state NMR.

Additional information

Author contributions

Conceptualization: J.D.V.S., M.W., and K.P.P.

Methodology: J.D.V.S., E.L.B., and M.W.

Investigation: J.D.V.S. and M.W.

Visualization: J.D.V.S.

Formal analysis: J.D.V.S. and M.W.

Software: J.D.V.S., E.L.B., and M.W

Supervision: K.P.P.

Writing—original draft: J.D.V.S.

Writing—review and editing: J.D.V.S., M.W., E.L.B., and K.P.P.

Funding

The authors acknowledge that they received no funding in support of this research.

Author ORCID iDs

Jason D van Schoor: https://orcid.org/0009-0007-0159-3353

References

1. **Sandhu SV,** Gupta S, Bansal H, Singla K (2012) Collagen in Health and Disease. *Journal of Orofacial Research* **2**:153-9 https://doi.org/10.5005/jp-journals-10026-1032 | PubMed
2. **Cieza A,** Causey K, Kamenov K, Hanson SW, Chatterji S, Vos T (2020) Global estimates of the need for rehabilitation based on the Global Burden of Disease study 2019: a systematic analysis for the Global Burden of Disease Study 2019. *The Lancet* **396**:2006-17 https://doi.org/10.1016/s0140-6736(20)32340-0 | PubMed
3. **Mohammed A,** Alshamarri T, Adeyeye T, Lazariu V, McNutt L-A, Carpenter DO (2020) A comparison of risk factors for osteo- and rheumatoid arthritis using NHANES data. *Preventive Medicine Reports* **20**:101242 https://doi.org/10.1016/j.pmedr.2020.101242 | PubMed
4. **Ouyang Z,** Dong L, Yao F, Wang K, Chen Y, Li S, et al. (2023) Cartilage-Related Collagens in Osteoarthritis and Rheumatoid Arthritis: From Pathogenesis to Therapeutics. *Int J Mol Sci* **24** https://doi.org/10.3390/ijms24129841 | PubMed
5. **Coelho NM,** McCulloch CA (2016) Contribution of collagen adhesion receptors to tissue fibrosis. *Cell and Tissue Research* **365**:521-38 https://doi.org/10.1007/s00441-016-2440-8 | PubMed
6. **Mutsaers HAM,** Merrild C, Nørregaard R, Plana-Ripoll O (2023) The impact of fibrotic diseases on global mortality from 1990 to 2019. *Journal of Translational Medicine* **21**:818 https://doi.org/10.1186/s12967-023-04690-7 | PubMed
7. **Wilson SL,** Guilbert M, Sulé-Suso J, Torbet J, Jeannesson P, Sockalingum GD, et al. (2014) A microscopic and macroscopic study of aging collagen on its molecular structure, mechanical properties, and cellular response. *The FASEB Journal* **28**:14-25 https://doi.org/10.1096/fj.13-227579 | PubMed
8. **Brodsky B,** Tanaka S, Eikenberry E. (1988) *X-Ray Diffraction as a Tool for Studying Collagen Structure* Collagen: CRC Press. pp. 95-112
9. **Hulmes DJ,** Jesior JC, Miller A, Berthet-Colominas C, Wolff C (1981) Electron microscopy shows periodic structure in collagen fibril cross sections. *Proc Natl Acad Sci U S A* **78**:3567-71 https://doi.org/10.1073/pnas.78.6.3567 | PubMed
10. **van Huizen NA,** Ijzermans JNM, Burgers PC, Luider TM (2020) Collagen analysis with mass spectrometry. *Mass Spectrometry Reviews* **39**:309-35 https://doi.org/10.1002/mas.21600 | PubMed
11. **Bielajew BJ,** Hu JC, Athanasiou KA (2020) Collagen: quantification, biomechanics and role of minor subtypes in cartilage. *Nature Reviews Materials* **5**:730-47 https://doi.org/10.1038/s41578-020-0213-1 | PubMed
12. **Mostaço-Guidolin L,** Rosin NL, Hackett T-L (2017) Imaging Collagen in Scar Tissue: Developments in Second Harmonic Generation Microscopy for Biomedical Applications. *International Journal of Molecular Sciences* **18** https://doi.org/10.3390/ijms18081772 | PubMed
13. **Mroue KH,** Nishiyama Y, Kumar Pandey M, Gong B, McNerny E, Kohn DH, et al. (2015) Proton-Detected Solid-State NMR Spectroscopy of Bone with Ultrafast Magic Angle Spinning. *Sci Rep* **5**:11991 https://doi.org/10.1038/srep11991 | PubMed
14. **Eliav U,** Navon G (2002) Multiple Quantum Filtered NMR Studies of the Interaction between Collagen and Water in the Tendon. *Journal of the American Chemical Society* **124**:3125-32 https://doi.org/10.1021/ja011791n | PubMed
15. **Ong HH,** Wright AC, Wehrli FW (2012) Deuterium nuclear magnetic resonance unambiguously quantifies pore and collagen-bound water in cortical bone. *Journal of Bone and Mineral Research* **27**:2573-81 https://doi.org/10.1002/jbmr.1709 | PubMed
16. **Laws DD,** Bitter H-ML, Jerschow A (2002) Solid-State NMR Spectroscopic Methods in Chemistry. *Angewandte Chemie International Edition* **41**:3096-129 https://doi.org/10.1002/1521-3773(20020902)41:17<3096::aid-anie3096>3.0.co;2-x | PubMed

17. **Seifert AC,** Li C, Rajapakse CS, Bashoor-Zadeh M, Bhagat YA, Wright AC, et al. (2014) Bone mineral 31P and matrix-bound water densities measured by solid-state 31P and 1H MRI. *NMR in Biomedicine* **27**:739-48 https://doi.org/10.1002/nbm.3107 | PubMed

18. **Seifert AC,** Wehrli FW (2016) Solid-State Quantitative (1)H and (31)P MRI of Cortical Bone in Humans. *Curr Osteoporos Rep* **14**:77-86 https://doi.org/10.1007/s11914-016-0307-2 | PubMed

19. **Horch RA,** Nyman JS, Gochberg DF, Dortch RD, Does MD (2010) Characterization of 1H NMR signal in human cortical bone for magnetic resonance imaging. *Magn Reson Med* **64**:680-7 https://doi.org/10.1002/mrm.22459 | PubMed

20. **Fantazzini P,** Brown RJS, Borgia GC (2003) Bone tissue and porous media: common features and differences studied by NMR relaxation. *Magnetic Resonance Imaging* **21**:227-34 https://doi.org/10.1016/s0730-725x(03)00129-2 | PubMed

21. **Edzes HT,** Samulski ET (1978) The measurement of cross-relaxation effects in the proton NMR spin-lattice relaxation of water in biological systems: Hydrated collagen and muscle. *Journal of Magnetic Resonance (1969)* **31**:207-29 https://doi.org/10.1016/0022-2364(78)90185-3

22. **Ma Y-J,** Chang EY, Bydder GM, Du J (2016) Can ultrashort-TE (UTE) MRI sequences on a 3-T clinical scanner detect signal directly from collagen protons: freeze-dry and D2O exchange studies of cortical bone and Achilles tendon specimens. *NMR in Biomedicine* **29**:912-7 https://doi.org/10.1002/nbm.3547 | PubMed

23. **Guo T,** Moazamian D, Suprana AA, Jerban S, Chang EY, Ma Y, et al. (2024) Are Collagen Protons Visible with the Zero Echo Time (ZTE) Magnetic Resonance Imaging Sequence: A D2O Exchange and Freeze-Drying Study. *Bioengineering* **12** https://doi.org/10.3390/bioengineering12010016 | PubMed

24. **Caravan P,** Das B, Dumas S, Epstein FH, Helm PA, Jacques V, et al. (2007) Collagen-targeted MRI contrast agent for molecular imaging of fibrosis. *Angew Chem Int Ed Engl* **46**:8171-3 https://doi.org/10.1002/anie.200700700 | PubMed

25. **Ma YJ,** Jerban S, Jang H, Chang D, Chang EY, Du J (2020) Quantitative Ultrashort Echo Time (UTE) Magnetic Resonance Imaging of Bone: An Update. *Front Endocrinol (Lausanne)* **11**:567417 https://doi.org/10.3389/fendo.2020.567417 | PubMed

26. **Chen J,** Grogan SP, Shao H, D'Lima D, Bydder GM, Wu Z, et al. (2015) Evaluation of bound and pore water in cortical bone using ultrashort-TE MRI. *NMR in Biomedicine* **28**:1754-62 https://doi.org/10.1002/nbm.3436 | PubMed

27. **Surowiec RK,** Ram S, Idiyatullin D, Goulet R, Schlecht SH, Galban CJ, et al. (2021) In vivo quantitative imaging biomarkers of bone quality and mineral density using multi-band-SWIFT magnetic resonance imaging. *Bone* **143**:115615 https://doi.org/10.1016/j.bone.2020.115615 | PubMed

28. **Weiger M,** Stampanoni M, Pruessmann KP (2013) Direct depiction of bone microstructure using MRI with zero echo time. *Bone* **54**:44-7 https://doi.org/10.1016/j.bone.2013.01.027 | PubMed

29. **Ni Q,** Nyman JS, Wang X, De Los Santos A, Nicolella DP (2007) Assessment of water distribution changes in human cortical bone by nuclear magnetic resonance. *Measurement Science and Technology* **18**:715 https://doi.org/10.1088/0957-0233/18/3/022

30. **Nyman JS,** Ni Q, Nicolella DP, Wang X (2008) Measurements of mobile and bound water by nuclear magnetic resonance correlate with mechanical properties of bone. *Bone* **42**:193-9 https://doi.org/10.1016/j.bone.2007.09.049 | PubMed

31. **Schreiner LJ,** Cameron IG, Funduk N, Miljković L, Pintar MM, Kydon DN (1991) Proton NMR spin grouping and exchange in dentin. *Biophys J* **59**:629-39 https://doi.org/10.1016/s0006-3495(91)82278-0 | PubMed

32. **Funduk N,** Kydon DW, Schreiner LJ, Peemoeller H, Miljković L, Pintar MM (1984) Composition and relaxation of the proton magnetization of human enamel and its contribution to the tooth NMR image. *Magn Reson Med* **1**:66-75 https://doi.org/10.1002/mrm.1910010108 | PubMed

33. **Englander SW,** Sosnick TR, Englander JJ, Mayne L (1996) Mechanisms and uses of hydrogen exchange. *Curr Opin Struct Biol* **6**:18-23 https://doi.org/10.1016/s0959-440x(96)80090-x | PubMed

34. **Froidevaux R,** Weiger M, Rösler MB, Brunner DO, Dietrich BE, Reber J, et al. (2020) High-resolution short-T2 MRI using a high-performance gradient. *Magn Reson Med* **84**:1933-46 https://doi.org/10.1002/mrm.28254 | PubMed

35. **Li C,** Magland JF, Rad HS, Song HK, Wehrli FW (2012) Comparison of optimized soft-tissue suppression schemes for ultrashort echo time MRI. *Magn Reson Med* **68**:680-9 https://doi.org/10.1002/mrm.23267 | PubMed

36. **Johnson EM,** Vyas U, Ghanouni P, Pauly KB, Pauly JM (2017) Improved cortical bone specificity in UTE MR Imaging. *Magn Reson Med* **77**:684-95 https://doi.org/10.1002/mrm.26160 | PubMed

37. **Szeverenyi NM,** Carl M (2012) *Contrast manipulation in MR imaging of short T2 and T2* tissues. Contrast manipulation in MR imaging of short T2 and T2* tissues, eMagRes* Chichester, United Kingdom: John Wiley & Sons, Ltd. pp. 581-6

38. **Rahmer J,** Börnert P, Groen J, Bos C (2006) Three-dimensional radial ultrashort echo-time imaging with T2 adapted sampling. *Magn Reson Med* **55**:1075-82 https://doi.org/10.1002/mrm.20868 | PubMed

39. **Ma YJ,** Jang H, Wei Z, Wu M, Chang EY, Corey-Bloom J, et al. (2021) Brain ultrashort T(2) component imaging using a short TR adiabatic inversion recovery prepared dual-echo ultrashort TE sequence with complex echo subtraction (STAIR-dUTE-ES). *Journal of Magnetic Resonance* **323**:106898 https://doi.org/10.1016/j.jmr.2020.106898 | PubMed

40. **Sobol WT,** Cameron IG, Inch WR, Pintar MM (1986) Modeling of proton spin relaxation in muscle tissue using nuclear magnetic resonance spin grouping and exchange analysis. *Biophysical Journal* **50**:181-91 https://doi.org/10.1016/s0006-3495(86)83450-6 | PubMed

41. **Belton PS,** Jackson RR, Packer KJ (1972) Pulsed NMR studies of water in striated muscle: I. Transverse nuclear spin relaxation times and freezing effects. *Biochimica et Biophysica Acta (BBA) - General Subjects* **286**:16-25 https://doi.org/10.1016/0304-4165(72)90084-0 | PubMed

42. **Ribeiro A,** Parello J, Jardetzky O (1984) NMR studies of muscle proteins. *Prog Biophys Mol Biol* **43**:95-160 https://doi.org/10.1016/0079-6107(84)90005-1 | PubMed

43. **Radoicic J,** Lu GJ, Opella SJ (2014) NMR structures of membrane proteins in phospholipid bilayers. *Q Rev Biophys* **47**:249-83 https://doi.org/10.1017/s0033583514000080 | PubMed

44. **McConnell HM** (1958) Reaction Rates by Nuclear Magnetic Resonance. *The Journal of Chemical Physics* **28**:430-1 https://doi.org/10.1063/1.1744152

45. **Vallurupalli P** (2009) *Chemical Exchange. Workshop Series on NMR and Related Topics, Homi Bhabha Centenary School on Relaxation in NMR and Related Aspects* Mumbai: TIFR.

46. **Ma YJ,** Chang EY, Carl M, Du J (2018) Quantitative magnetization transfer ultrashort echo time imaging using a time-efficient 3D multispoke Cones sequence. *Magn Reson Med* **79**:692-700 https://doi.org/10.1002/mrm.26716 | PubMed

47. **Brown SP,** Spiess HW (2001) Advanced Solid-State NMR Methods for the Elucidation of Structure and Dynamics of Molecular, Macromolecular, and Supramolecular Systems. *Chemical Reviews* **101**:4125-56 https://doi.org/10.1021/cr990132e | PubMed

48. **Baadsvik EL,** Weiger M, Froidevaux R, Schildknecht CM, Ineichen BV, Pruessmann KP (2024) Myelin bilayer mapping in the human brain in vivo. *Magn Reson Med* **91**:2332-44 https://doi.org/10.1002/mrm.29998 | PubMed

49. **Weiger M,** Pruessmann KP (2019) Short-T2 MRI: Principles and recent advances. *Prog Nucl Magn Reson Spectrosc* **114-115**:237-70 https://doi.org/10.1016/j.pnmrs.2019.07.001 | PubMed

50. **Venkatesh SK,** Yin M, Ehman RL (2013) Magnetic resonance elastography of liver: Technique, analysis, and clinical applications. *Magnetic Resonance Imaging* **37**:544-55 https://doi.org/10.1002/jmri.23731 | PubMed

51. **Chang EY,** Suprana A, Tang Q, Cheng X, Fu E, Orozco E, et al. (2024) Rotator cuff muscle fibrosis can be assessed using ultrashort echo time magnetization transfer MRI with fat suppression. *NMR in Biomedicine* **37**:e5058 https://doi.org/10.1002/nbm.5058 | PubMed

52. **Gudino N,** Littin S (2023) Advancements in Gradient System Performance for Clinical and Research MRI. *Magnetic Resonance Imaging* **57**:57-70 https://doi.org/10.1002/jmri.28421 | PubMed

53. **Weiger M,** Froidevaux R, Baadsvik EL, Brunner DO, Rösler MB, Pruessmann KP (2020) Advances in MRI of the myelin bilayer. *NeuroImage* **217**:116888 https://doi.org/10.1016/j.neuroimage.2020.116888 | PubMed

54. **Baadsvik EL,** Weiger M, Martinez Silberstein A, Luechinger R, Pruessmann KP. (2025) Towards faster myelin bilayer mapping: reducing the specific absorption rate at no cost. In: *Magnetic Resonance Materials in Physics, Biology and Medicine, Book of Abstracts ESMRMB 2025 Online 41st Annual Scientific Meeting 8–11 October 2025* Springer Nature. pp. 234 https://doi.org/10.1007/s10334-025-01278-8

55. **Jerban S,** Ma Y, Wan L, Searleman AC, Jang H, Sah RL, et al. (2019) Collagen proton fraction from ultrashort echo time magnetization transfer (UTE-MT) MRI modelling correlates significantly with cortical bone porosity measured with micro-computed tomography (μCT). *NMR Biomed* **32**:e4045 https://doi.org/10.1002/nbm.4045 | PubMed

56. **Hudson DM,** Archer M, Rai J, Weis M, Fernandes RJ, Eyre DR (2021) Age-related type I collagen modifications reveal tissue-defining differences between ligament and tendon. *Matrix Biology Plus* **12**:100070 https://doi.org/10.1016/j.mbplus.2021.100070 | PubMed

57. **Sołtysiak A,** Miśta-Jakubowska EA, Dorosz M, Kosiński T, Fijał-Kirejczyk I (2018) Estimation of collagen presence in dry bone using combined X-ray and neutron radiography. *Applied Radiation and Isotopes* **139**:141-5 https://doi.org/10.1016/j.apradiso.2018.03.024 | PubMed

58. **Schildknecht C,** Weiger M, Froidevaux R, Pruessmann K. (2021) Rapid high power transmit-receive switching using a timed cascade of PIN diodes. In: 29th Annual Meeting of ISMRM.

59. **Weiger M,** Overweg J, Viol A, Singenberger L, Schmid T, Baadsvik EL, et al. (2024) Making RF coils MR-invisible by additive manufacturing using magnetically filled polymer. In: ISMRM Singapore. https://doi.org/10.58530/2024/1564

60. **Grodzki DM,** Jakob PM, Heismann B (2012) Ultrashort echo time imaging using pointwise encoding time reduction with radial acquisition (PETRA). *Magn Reson Med* **67**:510-8 https://doi.org/10.1002/mrm.23017 | PubMed

61. **Weiger M,** Pruessmann KP (2023) Zero Echo Time (ZTE) MRI. In: Du J, Bydder GM (Eds). *MRI of Short- and Ultrashort-T2 Tissues: Making the Invisible Visible* Cham: Springer International Publishing. pp. 53-66 https://doi.org/10.1007/978-3-031-35197-6_5

62. **Balcom BJ,** Macgregor RP, Beyea SD, Green DP, Armstrong RL, Bremner TW (1996) Single-Point Ramped Imaging with T1 Enhancement (SPRITE). *Journal of Magnetic Resonance, Series A* **123**:131-4 https://doi.org/10.1006/jmra.1996.0225 | PubMed

63. **Schieban K,** Weiger M, Hennel F, Boss A, Pruessmann KP (2015) ZTE imaging with enhanced flip angle using modulated excitation. *Magn Reson Med* **74**:684-93 https://doi.org/10.1002/mrm.25464 | PubMed

64. **Pruessmann KP,** Weiger M, Börnert P, Boesiger P (2001) Advances in sensitivity encoding with arbitrary k-space trajectories. *Magn Reson Med* **46**:638-51 https://doi.org/10.1002/mrm.1241 | PubMed

65. **Tesiram YA** (2010) Implementation equations for HSn RF pulses. *Journal of Magnetic Resonance* **204**:333-9 https://doi.org/10.1016/j.jmr.2010.02.022 | PubMed

66. **Lee HM,** Weiger M, Giehr C, Froidevaux R, Brunner DO, Rösler MB, et al. (2020) Long-T2-suppressed zero echo time imaging with weighted echo subtraction and gradient error correction. *Magn Reson Med* **83**:412-26 https://doi.org/10.1002/mrm.27925 | PubMed

67. **Taye N,** Karoulias SZ, Hubmacher D (2020) The "other" 15–40%: The Role of Non-Collagenous Extracellular Matrix Proteins and Minor Collagens in Tendon. *Journal of Orthopaedic Research* **38**:23-35 https://doi.org/10.1002/jor.24440 | PubMed

68. **Augat P,** Schorlemmer S (2006) The role of cortical bone and its microstructure in bone strength. *Age and Ageing* **35**:ii27-ii31 https://doi.org/10.1093/ageing/afl081 | PubMed

69. Naomi R, Ridzuan PM, Bahari H (2021) Current Insights into Collagen Type I. *Polymers* **13** https://doi.org/10.3390/polym13162642 | PubMed

70. Krasnosselskaia LV. (2012) Mechanisms for Short T2 and T2* in Collagen-Containing Tissue. *eMagRes* **1** https://doi.org/10.1002/9780470034590.emrstm1278

71. Emid S, Creyghton JHN (1985) High resolution NMR imaging in solids. *Physica B+C* **128**:81-3 https://doi.org/10.1016/0378-4363(85)90087-7

Peer reviews

Reviewer #1 (Public review):

Summary:

The aim of this work is to directly image collagen in tissue using a new MRI method with positive contrast. The work presents a new MRI method that allows very short, powerful radio frequency (RF) pulses and very short switching times between transmission and reception of radio frequency signals.

Strengths:

The experiments with and without removal of 1H hydrogen, which is not firmly bound to collagen, on tissue samples from tendons and bones are very well suited to prove the detection of direct hydrogen signals from collagen. The new method has great potential value in medicine, as it allows for better investigation of ageing processes and many degenerative diseases in which functional tissue is replaced by connective tissue (collagen).

Comments on revisions:

All points of criticism in the reviews were answered very well and led to further improvement of the article.

https://doi.org/10.7554/eLife.109799.2.sa3

Reviewer #2 (Public review):

Summary:

This work presents direct magnetic resonance imaging (MRI) of collagen, which is not possible with conventional MRI or other tomographic imaging modalities.

Strengths:

The experimental work is impressive, and the presentation of results is clear and convincing.

https://doi.org/10.7554/eLife.109799.2.sa2

Reviewer #3 (Public review):

The paper is well written and well presented. The topic is important, and its significance is explained succinctly and accurately. I am only capable of reviewing the clinical aspects of this work which is very largely technical in nature. Several clinical points are worth considering:

(1) Tendons typically display large magic angle effects as a result of their highly ordered collagen structure (cortical bone much less so) and so it would have been of interest to know what orientation the tendons had to B 0 (in vitro and in vivo). This could affect the signal level at the longer echo time and thus the signal on the subtracted images.

(2) The in vivo transverse image looks about mid-forearm where tendons are not prominent. A transverse image of the lower forearm where there is an abundance of tendons might have been preferable.

(3) The in vivo images show the interosseous membrane as high signal on both the shorter and longer TE images. The structure contains ordered collagen with fibres at different oblique angles to the radius and ulnar and thus potentially to B 0. Collagen fibres may have been at an orientation towards the magic angle and this may account for the high signal on the longer TE image, and the low signal on the subtracted image.

(4) Some of the signals attributed to muscle may be from an attachment of the muscle to aponeurosis.

(5) There is significant collagen in subcutaneous tissues so the designation "skin" may more correctly be "skin and subcutaneous tissue".

(6) Cortical bone is very heterogeneous with boundaries between hard bone and soft tissue with significant susceptibility differences between the two across a small distance. This might be another mechanism for ultrashort T 2 * tissue values in addition to the presence of collagen. The two effects might be distinguished by also including a longer TE spin echo acquisition.

Solid cortical bone may also have an ultrashort T 2 * in its own right.

(7) It may be worth noting that in disease T 2 * may be increased. As a result, the subtraction image may make abnormal tissue less obvious than normal tissue. Magic angle effects may also produce this appearance.

(8) It may be worth distinguishing fibrous connective tissue (loose or dense) which may be normal or abnormal, from fibrosis which is abnormal accumulation of fibrous connective tissue in damaged tissue. Fibrosis typically has a longer T 2 initially and decreases its T 2 * over time. In places, the context suggests that fibrous connective tissue may be more appropriate than fibrosis.

Overall, the paper appears very well constructed and describes thoughtful and important work.

Comments on revisions:

The responses to my criticisms are well thought out and are fine as far as I am concerned.

I suggest in Figure 5 line 6 changing "trabecular bone" to "trabecular bone marrow".

https://doi.org/10.7554/eLife.109799.2.sa1

Author response:

The following is the authors' response to the original reviews

> ***Public Reviews:***
>
> ***Reviewer #1 (Public review):***
>
> *Summary:*

> *The aim of this work is to directly image collagen in tissue using a new MRI method with positive contrast. The work presents a new MRI method that allows very short, powerful radio frequency (RF) pulses and very short switching times between transmission and reception of radio frequency signals.*
>
> *Strengths:*
>
> *The experiments with and without the removal of 1H hydrogen, which is not firmly bound to collagen, on tissue samples from tendons and bones, are very well suited to prove the detection of direct hydrogen signals from collagen. The new method has great potential value in medicine, as it allows for better investigation of ageing processes and many degenerative diseases in which functional tissue is replaced by connective tissue (collagen).*
>
> *Weaknesses:*
>
> *It is clear that, due to the relatively long time intervals between RF excitation and signal readout, standard hardware in whole-body MRI systems can only be used to examine surrounding water and not hydrogen bound to collagen molecules.*

We agree that this is a regrettable situation (see also Discussion section). We are hoping that current and future efforts of MRI manufacturers towards improved hardware will eventually enable the technique for broader application.

> ***Reviewer #2 (Public review):***
>
> *Summary:*
>
> *This work presents direct magnetic resonance imaging (MRI) of collagen, which is not possible with conventional MRI or other tomographic imaging modalities.*
>
> *Strengths:*
>
> *The experimental work is impressive, and the presentation of results is clear and convincing. Through a series of thoughtfully prepared experiments, I found the evidence that the images reflect direct measurements of collagen to be highly compelling.*

Due to the technical demands, direct collagen imaging is unlikely to become widespread for routine clinical work, at least not anytime soon. That said, this work is nonetheless transformative and will likely be highly significant for research and perhaps clinical trials.

> ***Reviewer #3 (Public review):***
>
> *The paper is well written and well presented. The topic is important, and its significance is explained succinctly and accurately. I am only capable of reviewing the clinical aspects of this work, which is very largely technical in nature. Several clinical points are worth considering:*
>
> *(1) Tendons typically display large magic angle effects as a result of their highly ordered collagen structure (cortical bone much less so), and so it would have been of interest to know what orientation the tendons had to B 0 (in vitro and in vivo). This could affect the signal level at the longer echo time and thus the signal on the subtracted images.*

We have added arrows in the images showing the direction of the main magnetic field. For the in vivo case, the subject lay in the superman position, with B0 pointing from the hand towards the shoulder.

> *(2) The in vivo transverse image looks about mid-forearm, where tendons are not prominent. A transverse image of the lower forearm, where there is an abundance of tendons, might have been preferable.*

We have added a distal view of the forearm, where more tendon structures are observed.

> *(3) The in vivo images show the interosseous membrane as a high signal on both the shorter and longer TE images. The structure contains ordered collagen with fibres at different oblique angles to the radius and ulnar, and thus potentially to B 0. Collagen fibres may have been at an orientation towards the magic angle, and this may account for the high signal on the longer TE image and the low signal on the subtracted image.*

This is certainly an interesting take. While the magic angle effect is well established for collagen bound water, the orientation effects on the macromolecular collagen signal are still to be investigated. Our initial experiences so far suggest that the direct collagen signal is not as sensitive to orientation as the bound water.

Regarding the described observation for the interosseous membrane, we expect the high signal coming from collagen-bound water (yet not quite at the magic angle), which hardly decays between the two TEs, as their difference is small as compared to the T2* of this signal. Hence, this signal is removed in the subtraction image, and only the macromolecular collagen signal remains, which appears to be very low. Working with samples of the interosseus membrane may provide further insights into why this is the case.

> *(4) Some of the signals attributed to the muscle may be from an attachment of the muscle to the aponeurosis.*

We have added the aponeurosis as a possible signal contributor in the muscle tissue.

> *(5) There is significant collagen in subcutaneous tissues, so the designation "skin" may more correctly be "skin and subcutaneous tissue".*

We have updated the label accordingly.

> *(6) Cortical bone is very heterogeneous, with boundaries between hard bone and soft tissue with significant susceptibility differences between the two across a small distance. This might be another mechanism for ultrashort T 2 * tissue values in addition to the presence of collagen. The two effects might be distinguished by also including a longer TE spin echo acquisition.*

Solid cortical bone may also have an ultrashort T 2 * in its own right.

The described effect is clearly of importance for bone water but plays a negligible effect for the macromolecular signal. We would like to support this by a brief, coarse estimation. T_2* can be approximated by $1/T_2^* = 1/T_2 + 1/T_2'$, where $1/T_2' = \gamma \Delta B = \gamma \Delta \chi B_0$ (Ref. 1).

The susceptibilty difference reported for the interface between bone and water is $\Delta\chi$ = 2.5 ppm (Refs. 2 and 3), which at 3T leads to a $T_2' \approx 3000\ \mu s$. From our recorded FIDs, we use a T_2* of 10 µs and thus obtain $T_2 = 10.03\ \mu s$.

As can be seen, the change in the transverse relaxation constant due to susceptibility is negligible compared to the intrinsic decay of the macromolecular collagen signal. Notably, this is not the case for the pore water signal where T_2s are on the order of milliseconds (Ref. 2).

A footnote was added in the Introduction section regarding this topic.

> *(7) It may be worth noting that in disease T 2 * may be increased. As a result, the subtraction image may make abnormal tissue less obvious than normal tissue. Magic angle effects may also produce this appearance.*

This is an important point regarding image interpretation. For this reason, it is advantageous that also the original anatomical images prior to subtraction are available, which will show such effects. They can be used in conjuction with the collagen-specific image to provide further insights regarding tissue disease. Increased T_2* of diseased tissue has so far been reported for the bound water components due to a reduction of dipolar interactions between bound water and collagen (Ref. 4). A potential related change in T_2 for the macromolecular collagen component itself is certainly of interest and an avenue to explore in future work.

> *(8) It may be worth distinguishing fibrous connective tissue (loose or dense), which may be normal or abnormal, from fibrosis, which is an abnormal accumulation of fibrous connective tissue in damaged tissue. Fibrosis typically has a longer T 2 initially and decreases its T 2 * over time. In places, the context suggests that fibrous connective tissue may be more appropriate than fibrosis.*

We are aware of this important distinction. We therefore checked the manuscript for references to fibrosis, making sure that the meaning is as intended.

> *Overall, the paper appears very well constructed and describes thoughtful and important work.*
>
> ***Recommendations for the authors:***
>
> ***Reviewer #1 (Recommendations for the authors):***
>
> *(1) It should be stated that various methods with very short echo times (e.g. SWIFT by Garwood et al.) have been described in the past. This work shows for the first time that direct signals from collagen and be systematically detected in tissue samples.*

We have expanded a sentence in the introduction and reference selected publications studying short-T_2 water signal in collagen, including SWIFT.

> *(2) It should be noted that the 1H atoms bound to collagen are located at different sites (at different amino acids of the protein) of the molecule and have different frequencies, and that further signal analyses are of interest.*

We have included additional information regarding distinct resonances of proton-binding sites of collagen in the introduction. The discrete observation of such signals requires advanced NMR methodology such as magic-angle spinning and RF decoupling, which is not a suitable approach for in vivo MRI. Without such methods, the broad lineshapes overlap strongly and are rather observed as a single decaying exponential with the dipolar oscillation as we observe in the FIDs.

> *(3) Is it certain that the bump at 30 microseconds comes from 'dipolar coupling'? Is the development time probably too short for chemical shift-induced interference or J-coupling effects?*

30 microseconds is an extremely short interval to accumulate phase and requires large resonance offsets to observe significant changes. To investigate the nature of the bump, we also collected data on a Bruker 7T NMR spectrometer (see Author response image 1). Overall the same signal characteristics are observed as with 3T. In particular, the position of the bump is the same, excluding chemical shift as as source. However, with the higher field strength, chemical shift becomes significant for the signal phase, as observed by the change in the phase behavior at 50 microseconds, when the collagen component has decayed.

While J-coupling is independent of field strength, the typical ranges are single-digit to tens of Hertz. In contrast, dipolar coupling interacts on the order of thousands of Hertz, which coincides with the values extracted from our signal model.

To clarify this point, we extended the respective sentence in the Results section.

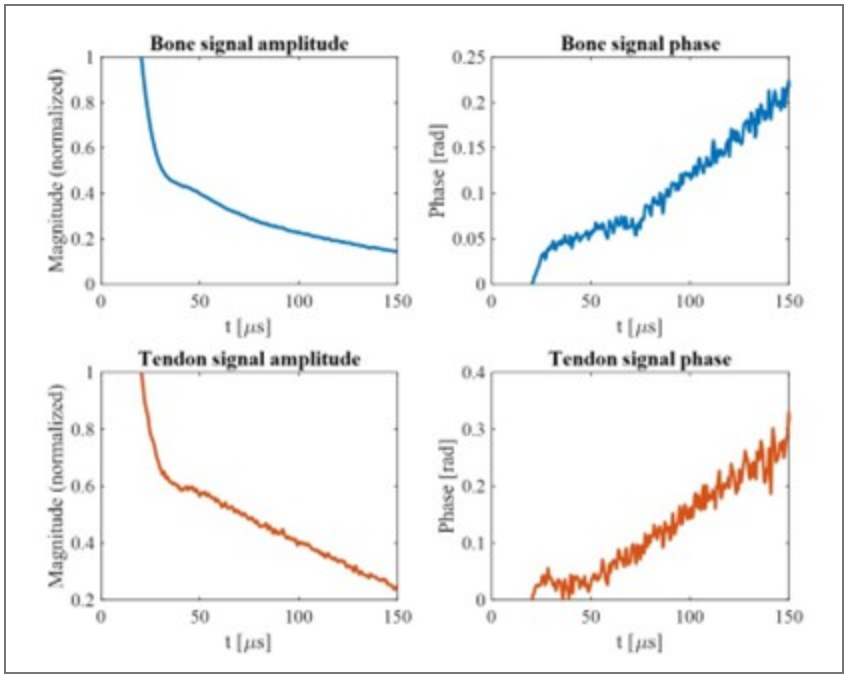

Author response image 1.

> *(4) It should be noted that short RF pulses have a relatively high energy content, and whether there are any particular stresses on patients during the examination (SAR, nerve stimulation?).*

SAR is an important issue in ZTE MRI. Since imaging bandwidths are large and excitation is performed with the imaging gradient being on, broadband pulses are necessary. Hence, significant RF deposition occurs and in vivo the flip angle can often not be optimized for the maximum signal, but will be limited by the SAR limit. We have added an explanation in the Discussion section.

Peripheral nerve stimulation is generated by rapid switching of strong gradients. However, ZTE sequences are usually operated without switching gradients on and off, but with only minor adjustments of the gradient direction between TR intervals. Therefore, PNS is not a relevant issue.

> *(5) In the Results section, Part B, 'substantial signal intensity' should be written instead of 'substantial image intensity'.*

We have changed this as suggested.

References

(1) Chavhan GB, Babyn PS, Thomas B, Shroff MM, Haacke EM. Principles, techniques, and applications of T2*-based MR imaging and its special applications. Radiographics. 2009 Sep-Oct;29(5):1433-49. doi: 10.1148/rg.295095034. PMID: 19755604; PMCID: PMC2799958.

(2) Seifert, AC, Wehrli, SL, and Wehrli, FW (2015), Bi-component T_2* analysis of bound and pore bone water fractions fails at high field strengths. NMR Biomed., 28, 861– 872. doi: 10.1002/nbm.3305.

(3) Hopkins JA, Wehrli FW. Magnetic susceptibility measurement of insoluble solids by NMR: magnetic susceptibility of bone. Magn Reson Med. 1997 Apr;37(4):494-500. doi: 10.1002/mrm.1910370404. PMID: 9094070.

(4) Loegering IF, Denning SC, Johnson KM, Liu F, Lee KS, Thelen DG. Ultrashort echo time (UTE) imaging reveals a shift in bound water that is sensitive to sub-clinical tendinopathy in older adults. Skeletal Radiol. 2021 Jan;50(1):107-113. doi: 10.1007/s00256-020-03538-1. Epub 2020 Jul 8. PMID: 32642791; PMCID: PMC7677198.

https://doi.org/10.7554/eLife.109799.2.sa0